THE CHOOZ EXPERIMENT

PROPOSAL TO SEARCH FOR NEUTRINO VACUUM OSCILLATIONS TO $\Delta m^2 = 10^{-3}$ eV^2 USING A 1 KM BASELINE REACTOR NEUTRINO EXPERIMENT

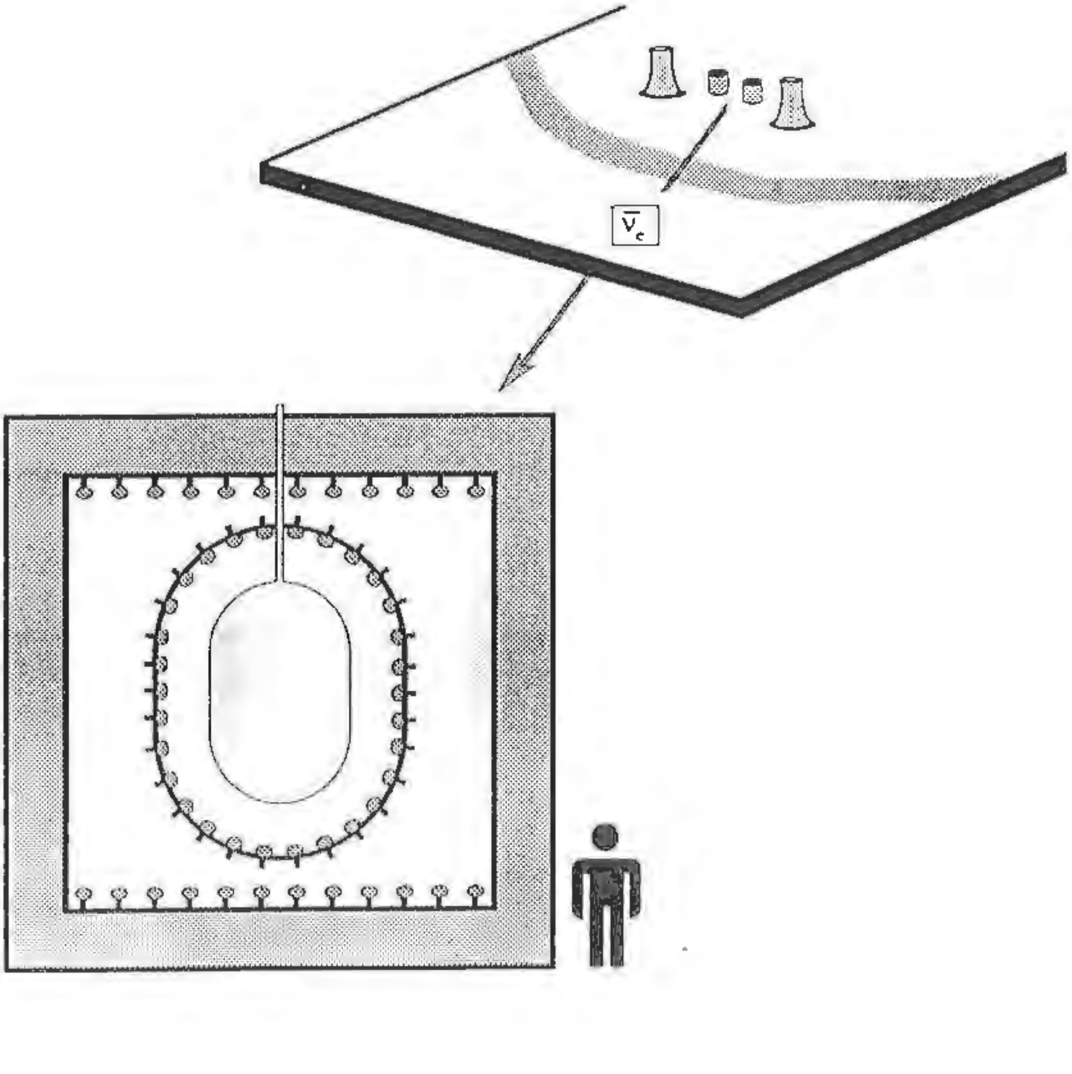

PROPOSAL TO SEARCH FOR NEUTRINO VACUUM OSCILLATIONS TO $\Delta m^2 = 10^{-3} eV^2$ USING A 1 KM BASELINE REACTOR NEUTRINO EXPERIMENT

April 1993

The Chooz Collaboration

Collège de France:	*H. de Kerret, D. Kryn, B. Lefièvre, M. Obolensky, S. Sukhotin, P. Courty and D. Marchand*
Drexel University:	*R. Steinberg*, C.E. Lane and F.C. Wang*
Kurchatov Institute:	*V.P. Martemyanov, L.A. Mikaelyan, M.D. Skorokhvatov, and V.N. Vyrodov*
LAPP (Annecy):	*Y. Declais*. J. Favier and A. Oriboni*
Univ. of California (Irvine):	*Z.D. Greenwood, W.R. Kropp. L. Price, S. Riley and H. Sobel*
Univ. of New Mexico:	*B.B. Dieterle and R. Reeder*

*Co-spokesmen

Contents

List of Figures

List of Tables

Chapter 1

Introduction

One of the central issues in particle physics, as well as in astrophysics and cosmology, is the question of whether or not the rest masses of the neutrinos are exactly zero. In the minimal $SU(2)_L \otimes U(1)$ standard electroweak model, all neutrinos are massless and lepton number is exactly conserved. Despite long-standing success, however, the standard model is incomplete and inadequate, with many parameters left unspecified and a physically unreasonable global symmetry needed to enforce exact lepton number conservation.

The standard model, therefore, is generally agreed to need significant extensions. Although the nature of the necessary modifications is unclear, most proposed extensions of the standard model allow finite neutrino mass and many others require it. Experimental searches for neutrino mass are therefore important both to test the standard model and to guide theorists seeking a better model. Clear experimental evidence for finite neutrino mass would herald a new era of physics "beyond the standard model".

Furthermore, if the neutrinos are experimentally proven to have mass, not only would there be deep implications for our theoretical ideas on particle physics and on the unification of forces, but also for our understanding of essential astrophysical phenomena such as the energy generating mechanism of the Sun, the final stages of stellar evolution, and the history of the Universe itself. Thus, the experimental search for finite neutrino mass could well provide the key to a rich domain of new phenomena.

We are proposing here an incisive new experiment combining and extending proven methods of particle detection and background rejection to search with order-of-magnitude improved sensitivity for the phenomenon of neutrino oscillations. If discovered, such oscillations would provide clear proof of the existence of finite neutrino mass.

This area is ripe for a new and potentially definitive experiment, in that experimental hints for the existence of neutrino oscillations come from two distinct sets of observations: a long series of unexpectedly low results in measurements of the terrestrial flux of solar neutrinos; and the observation of an anomaly in the flux of cosmic-ray produced muon neutrinos observed by deep underground detectors. Achieving sensitivity to the neutrino mass scales indicated by these hints requires a new generation of long baseline neutrino oscillation experiments such as the experiment we here propose.

There are a number of experimental approaches to detection of a finite neutrino rest mass. Precision measurements of low energy beta decay spectra in the vicinity of their end points (*i.e.* zero neutrino kinetic energy) offer perhaps the most direct approach. Current mass limits provided by this technique, however, are not very sensitive. Even in the most favorable case of electron antineutrinos, experiments have been able to attain sensitivity limits of only about 10 eV.

Other methods sensitive to smaller neutrino masses include investigation of the time structure of neutrino pulses from collapsing stars, probing for neutrinoless $\beta\beta$ decay, and searching for neutrino matter and vacuum oscillations. Since oscillation experiments make use of a quantum mechanical interference effect, they have the advantage of potentially exquisite sensitivity to the mass differences of the oscillating particles. For example, the observed strangeness oscillations in the K^0-$\overline{K}^0$ system reveal an underlying mass difference of $\Delta m = 3.5 \times 10^{-6}\,\text{eV}$!

The Chooz experiment which we propose here makes use of the oscillation technique to perform a very sensitive search for extremely small neutrino masses.

In Chapter 2 we review the current status of neutrino oscillation experiments, emphasizing the experimental hints that exist for the presence of neutrino oscillations.

Chapters 3 and 4 present an overview of the Chooz experiment and a detailed discussion of its design. In Chapter 5 we treat the Chooz electronics, and in Chapter 6 the planned calibration procedures. Chapters 7 and 8 concern the expected performance of the detector for neutrino events and for the background, respectively.

Chapter 2

Neutrino Oscillations

If at least one neutrino has a finite rest mass and if the separate lepton numbers L_e, L_μ, and L_τ are not exactly conserved in nature, it is likely that the neutrino flavor eigenstates, ν_l, (where $l = e, \mu, \tau$) produced by the weak interaction would not be identical with the true neutrino mass eigenstates ν_i, but would consist of a linear combination of the ν_i. That is,

$$\nu_l = \sum_i U_{li} \nu_i \ ,$$

where U_{li} is known as the mass eigenstate mixing matrix. If the off-diagonal components of this matrix were non-zero, mixing among the flavor eigenstates would exist and the various neutrino species would evolve in time as linear combinations of mass eigenstates.

This intriguing phenomenon, known as neutrino oscillations, was first propounded by Pontecorvo [1] in the context of ν_e-$\overline{\nu}_e$ transitions, well before the discovery of additional neutrino flavors. Maki *et al.* [2] were the first to discuss neutrino flavor oscillations of the type of interest here.

For the simple case of oscillations between neutrinos of the flavors e and μ, the above equation becomes

$$\begin{pmatrix} \nu_e \\ \nu_\mu \end{pmatrix} = \begin{pmatrix} \cos\theta \ \sin\theta \\ -\sin\theta \ \cos\theta \end{pmatrix} \begin{pmatrix} \nu_1 \\ \nu_2 \end{pmatrix} \ .$$

For an initially pure ν_e state, the ν_μ amplitude evolves at time t to

$$\nu_\mu(t) = -\nu_1 \sin\theta \, e^{-iE_1 t} + \nu_2 \cos\theta \, e^{-iE_2 t} \ ,$$

and the probability of finding a ν_μ at distance $L = ct$ becomes

$$P_{\nu_\mu} = \sin^2 2\theta \, \sin^2 \left[\frac{1.27 \Delta m^2 L}{E_\nu} \right] \ ,$$

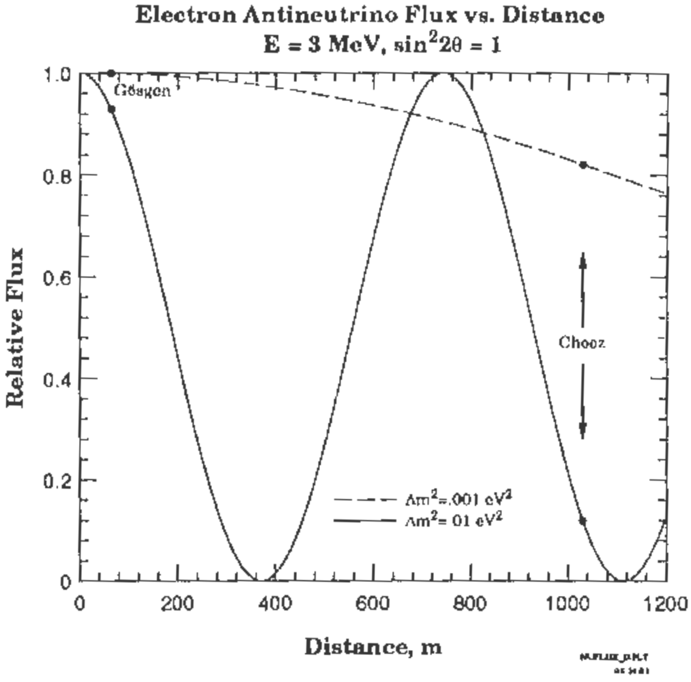

Figure 2.1: Neutrino flux vs. distance for a monochromatic 3 MeV $\overline{\nu}_e$ beam at Gösgen and Chooz for maximal mixing at two different values of Δm^2. For Δm^2 as low as $10^{-3}\,\mathrm{eV}^2$, the neutrino flux reduction at Chooz would be a readily observable 20%.

where $\Delta m^2 = m^2_{\nu_e} - m^2_{\nu_\mu}$ in eV^2, L is the distance in meters and E_ν is the neutrino energy in MeV. If we have a detector sensitive only to ν_e , then the observed count rate will be proportional to

$$P_{\nu_e} = 1 - P_{\nu_\mu} = 1 - \sin^2 2\theta \sin^2\left[\frac{1.27\Delta m^2 L}{E_\nu}\right] .$$

This result applies to a situation where the neutrinos have a single energy and where the neutrino source and detector are point-like. The observed count rate will thus oscillate between 1 and $1-\sin^2 2\theta$, as shown in Fig. 2.1. In the case of a non-monochromatic source or non-pointlike geometry, the oscillation amplitude will be reduced. In extreme cases, P_{ν_e} will reach a constant equilibrium value of $1 - \frac{1}{2}\sin^2 2\theta$.

In an experiment searching for neutrino oscillations, the overarching measure of quality is the ability to discern small values of $\sin^2 2\theta$ and Δm^2. With respect to the latter, large values of L and small values of E_ν are required. The proposed Chooz experiment attains its high sensitivity by doing both, reaching an L/E_ν ratio of about 500 m/MeV, an order of magnitude higher than in previous laboratory-quality measurements.

The results of neutrino oscillation experiments are usually plotted on graphs of Δm^2 vs. $\sin^2 2\theta$, in which regions excluded (or *included*, in the event of a discovery) are delineated by contours at various confidence levels, usually 90% (1.645σ). Examples of such "exclusion plots" are shown in Figs. 2.3 and 2.4.

2.1 Experimental Hints

2.1.1 Solar Neutrinos

^{8}B Neutrinos – Homestake and Kamiokande II

For over twenty years, a radiochemical ^{37}Cl neutrino experiment in the Homestake Gold Mine [3] has been monitoring the flux of relatively high energy neutrinos (thought to be mainly from ^{8}B decays in the Sun) with a count rate consistently about a factor of three below the value expected from standard models of solar physics [4, 5]. Apparently, either our models of the Sun's interior are incomplete or our understanding of neutrino physics is deficient. Calculated values for the Homestake chlorine experiment are in the range 6–8 SNU (1 solar neutrino unit = 10^{-36} captures/target atom/second), while the measured $\nu_e + {}^{37}\mathrm{Cl} \rightarrow {}^{37}\mathrm{Ar} + e^-$ production rate is 2.3 ± 0.3 SNU (0.44 ± 0.05 captures/day) after subtracting a terrestrial background of 0.4 ± 0.2 SNU.

The low flux at Homestake has been confirmed by Kamiokande II [6], a 1000 ton water Čerenkov detector which uses the neutrino-electron elastic scattering reaction to measure the ^{8}B recoil electron spectrum. The observed recoil electron angular distribution is shown in Fig. 2.2 together with the expected distribution based on the Bahcall-Ulrich standard solar model prediction [4]. The peak in Fig. 2.2 gives a clear indication of an excess signal *from the direction of the Sun* corresponding to a flux

$$0.46 \pm 0.05(\mathrm{stat}) \pm 0.06(\mathrm{syst})$$

times that of the standard solar model.

Proton-Proton Neutrinos – SAGE and GALLEX

In the standard solar model, more than 99% of the terminations of the proton-proton chain lead to emission of an electron neutrino with energy less than 0.42 MeV. ^{71}Ga, with a threshold of 0.23 MeV, is so far the only feasible target material capable of detecting the intense flux of these low-energy *p-p* neutrinos. Using the standard solar model, the total counting rate in gallium, including all reactions, is expected to be 132 SNU, corresponding to 2 counts/day in a 60 ton experiment.

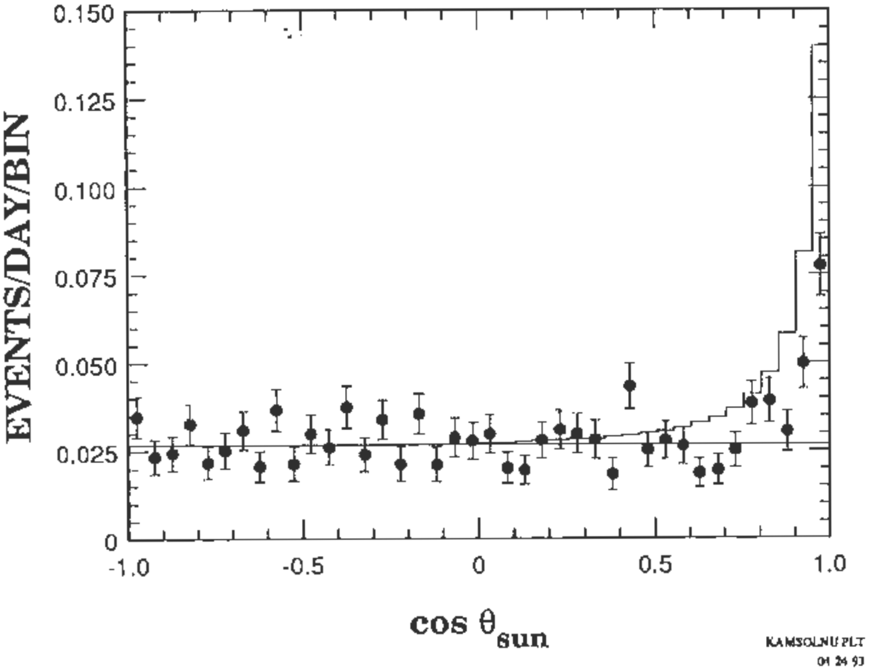

Figure 2.2: Measured Kamiokande II recoil electron angular distribution after 1040 live detector days (from ref. [6]). The independent variable is the angle between the reconstructed electron direction and the Sun. The plot clearly shows an isotropic background plus an excess of events from the direction of the Sun. The solid histogram shows the expected distribution using a Monte Carlo simulation based on the standard solar model.

Two ^{71}Ga experiments are currently in operation. The first is the 60 ton Soviet American Gallium Experiment (SAGE) at Baksan [7], which has recently reported a signal level of $58^{+17}_{-24} \pm 14$ SNU. The second is the 30 ton GALLEX experiment at Gran Sasso [8], which sees $83 \pm 19 \pm 8$ SNU. The two results are consistent, and both suggest a neutrino flux level low compared to the total expected from standard solar model calculations. The results are not yet good enough to be able to make a strong case, however, for flux levels lower than the p-p prediction. Assuming the experiments are correct (neutrino source calibrations are planned for both SAGE and GALLEX in the near future), it is not at all clear whether the answer lies with the neutrino physics, solar physics, or a combination of both [9, 10, 11].

Interpretation of Solar Neutrino Results

The flux of the high energy ^{8}B neutrinos to which the chlorine and water experiments are most sensitive is critically dependent on the temperature of the Sun's core. To calculate the ^{37}Ar production rate to within a factor of ~ 3, the solar core temperature must be known to an accuracy of $\sim 5 - 10\%$. Numerous non-standard solar models [12] have therefore been suggested, incorporating a variety of heavy metal abundances, high magnetic fields, turbulent diffusion, continuous mixing, rapidly rotating or burned-out helium cores, convective mixing of hydrogen into the core, or new equations of state. All of these effects go in the direction of lowering the solar core temperature. However, these non-standard models generally have difficulties accounting for other observed features of the Sun.

In addition to solar model effects, it has also been suggested that our understanding of the relevant particle physics may be incomplete. Mikheyev and Smirnov [13] and Wolfenstein [14] have pointed out that the different couplings of ν_e, ν_μ, and ν_τ to matter can cause an oscillation effect. If $\nu_{e,\mu,\tau}$ are orthogonal linear combinations of the same mass eigenstates, then ν_e produced by ^{8}B decays in the solar core can oscillate into ν_μ or ν_τ as they propagate outward through the Sun's overlying layers. Since the chlorine detector is insensitive to ν_μ and ν_τ (and water only weakly sensitive), the Homestake and Kamiokande rates would be suppressed. Over the range of neutrino mass differences $\Delta m^2 \sim 10^{-7} - 10^{-4}\,\mathrm{eV}^2$ and vacuum mixing angles $\sin^2 2\theta \sim 10^{-4} - 1$, the counting rate suppression could be just the required factor of $2 - 4$.

Neutrino magnetic moments, transition moments, neutrino decays, as well as weakly interacting massive particles and nuclei with extra quarks in the solar core have also been invoked as possible causes of the solar neutrino problem.

If we interpret the deficit of solar neutrinos as being due to the oscillation of $\nu_e \rightarrow \nu_\mu$, then this observation can be used in conjunction with the seesaw mechanism [15] to set a scale for neutrino masses. For example, if these experiments imply that Δm^2 is in the range 10^{-4} to $10^{-8}\,\mathrm{eV}^2$, then the seesaw mechanism would yield

$$m_{\nu_\mu} = 10^{-2} \text{ to } 10^{-4}\,\mathrm{eV}$$

and

$$m_{\nu_\tau} = 3 \text{ to } 3 \times 10^{-2}\,\mathrm{eV},$$

implying that $\Delta m^2_{\nu_e - \nu_\tau} = 1 \times 10^1$ to $1 \times 10^{-3}\,\mathrm{eV}^2$. Further, if lepton mixing roughly corresponds with the corresponding quark mixing, we would have

$$\sin^2 2\theta \sim 10^{-4} \text{ for } \nu_e - \nu_\tau$$

$$\sin^2 2\theta \sim 10^{-2} \text{ for } \nu_\mu - \nu_\tau$$

and

$$\sin^2 2\theta \sim 10^{-1} \text{ for } \nu_e \to \nu_\mu \quad .$$

2.1.2 Atmospheric Neutrinos

Atmospheric neutrinos are produced by the interaction of primary cosmic rays in the atmosphere. These neutrinos penetrate the Earth and arrive almost isotropically at large underground detectors, having traveled distances from ~ 10 km (when coming directly from above) to ~ 12000 km (coming from below). These large distances, together with the relatively low mean energy of the neutrinos, provide an opportunity to study oscillations to very low values of Δm^2.

Oscillation studies with atmospheric neutrinos have several drawbacks, however, limiting their sensitivity to large mixing angles. The flux is composed of roughly equal proportions of electron and muon neutrinos and antineutrinos. This composition makes an appearance experiment impractical. Moreover, the energy spectrum is mostly below charged current τ threshold, so oscillation to ν_τ would manifest itself only as a loss of muon neutrinos. Finally, the low energy spectrum creates problems with the interpretation of the data. This energy region, while in principle well understood theoretically, involves mainly quasi-elastic and resonance production processes, in which numerous resonances are either not well established or have form-factors which have not been measured accurately. In addition, the interactions in the detector take place mainly within oxygen nuclei, which makes modeling difficult.

Nevertheless, large samples of contained neutrino interactions have been analyzed for the presence of neutrino oscillations.

Neutrino Events Contained within the Detector

The most accurately predicted feature of atmospheric neutrinos, (± 5%), is the ratio of the muon neutrino flux to that of the electron neutrinos. If oscillations of any kind take place, this ratio could change.

To study this effect it is necessary to identify the leptons produced in the neutrino interactions, namely to be able to differentiate between muon and electron signals. There are two methods for accomplishing this task:

- Muon decay signature identification. In the IMB-3 detector, the observed muon decay fraction was about 2σ below expectation.
- Lepton identification using "showering" vs. "non-showering" tracks. In the visible energy range 100 - 1500 MeV, the IMB-3 detector observed a non-showering fraction (muons) which was $3\sigma_{stat}$ below the expected fraction [16].

A similar deficit has been reported by the Kamiokande detector, which also measured an anomalously low non-showering fraction [17]. Neither IMB nor

Kamiokande observed a correlation of this deficit with energy or angle (neutrino path-length) as one might expect from oscillations. Nevertheless, the Kamiokande deficit has been interpreted as a manifestation of muon neutrino oscillations with a most probable Δm^2 of $10^{-2}\,\mathrm{eV}^2$ and with a mixing as high as $\sin^2 2\theta \sim 0.69$ [18].

Neutrinos Interacting Beneath the Detector

Another source of information for oscillation studies was provided by neutrinos which interacted in the rock and produced secondary particles (mainly muons) which entered the detector from below. Computer simulations based on a variety of flux, interaction and transport models predicted the rates and energy spectra. No significant deviations were seen.

The sensitivity to mixing angle in these analyses was limited mainly by the 20% systematic uncertainty in the flux. To overcome this limitation, the detectors studied the flux-independent ratio of the rate of up-going tracks stopping in the detector to the rate of exiting tracks. Since the median energy of stopping muons is 5 GeV while that of exiting muons is 80 GeV, the ratio is sensitive to oscillations. The measured value was in good agreement with the predicted value (depending on the model applied). Again, no evidence for oscillation was seen.

These intriguing observations constitute the "atmospheric neutrino anomaly" and richly deserve further study. See Fig. 2.3.

2.1.3 Single Solution to the Atmospheric and Solar Neutrino Anomalies

An interesting analysis has been offered [19] which tries to find a common solution to the two neutrino puzzles. The anomalously low ratio of the atmospheric ν_μ flux to ν_e flux at low energies is attributed to $\nu_\mu \leftrightarrow \nu_e$ mixing. The lack of similar depletion of the high energy upward-going ν_μ flux is explained in this model by suppression of the vacuum mixing factor $\sin^2(2\theta_V)$ due to matter effects in the Earth [20]. A further consequence of this model is the energy-independent depletion of solar neutrinos to about 60% of the predicted flux in radiochemical experiments and to about 66% in ν-e scattering experiments. With three-family mixing, values as low as 33% are obtained, thus explaining the long-standing solar neutrino deficit. The oscillation parameters suggested by this analysis are $\Delta m_V^2 \sim (0.5 - 1.4) \times 10^{-2}\,\mathrm{eV}^2$ and $\sin^2(2\theta_V) \sim 0.8$, which easily fall within the range of Chooz.

This analysis illustrates the possible existence of new physics in the domain between $10^{-2}\,\mathrm{eV}^2$ and $10^{-3}\,\mathrm{eV}^2$, the region of interest for the present proposal.

2.2 Neutrino Oscillation Experiments at Reactors

2.2.1 Motivation

As we have seen by combining the results from atmospheric and solar neutrinos, the largely unexplored $\Delta m^2 - \sin^2 2\theta$ region between $\Delta m^2 \sim 10^{-2}\,\mathrm{eV}^2$ and $10^{-4}\,\mathrm{eV}^2$ is extremely interesting. Further, as we have shown, the solar neutrino results, when combined with the seesaw mechanism, imply that a search for $\nu_e \rightarrow \nu_x$ oscillations in this region may be crucial.

Since sensitivity to low-mass neutrino oscillations requires a large value of L/E_ν, large and costly experiments have been envisaged using GeV *accelerator* neutrino beams and very long distances (hundreds of kilometers) to achieve a Δm^2 sensitivity approaching $\sim 10^{-3}\,\mathrm{eV}^2$. An experiment using *reactor* neutrinos has the major advantage that the average neutrino energy is very low ($\sim 2\,\mathrm{MeV}$), a factor of 1000 lower than the energy of typical accelerator neutrino beams. Therefore, to achieve the same Δm^2 sensitivity, shorter distances and much smaller, less costly experiments are required.

In this document, we propose a new reactor neutrino oscillation experiment to achieve a sensitivity of $\Delta m^2 = 10^{-3}\,\mathrm{eV}^2$. In addition, the experiment proposed here will contribute toward the design of later experiments capable of sensitivities down to $\sim 10^{-4}\,\mathrm{eV}^2$ and possibly beyond.

2.2.2 Previous Reactor Experiments

Nuclear power reactors provide intense, rather well understood sources of low energy $\overline{\nu}_e$'s. Not only is the neutrino energy spectrum known to an accuracy of a few percent, but the neutrino flavor composition (pure $\overline{\nu}_e$) and angular distribution (isotropic) of the reactor neutrino beam are known essentially perfectly, unlike accelerator neutrino beams. Thus, reactors provide nearly ideal sources for neutrino oscillation experiments.

Over the years, therefore, a number of neutrino oscillation searches have been performed. Table 2.1 compares a number of these experiments, as well as three future experiments.

The best present limits from a reactor neutrino oscillation measurement come from an experiment led by F. Boehm at Gösgen in Switzerland which was 65 meters from the reactor and achieved a Δm^2 sensitivity approaching $\sim 10^{-2}\,\mathrm{eV}^2$ [23]. A more stringent limit in Δm^2 has been obtained recently by a Kurchatov Institute group [26], but the sensitivity in mixing was not as good ($\sin^2 2\theta \sim .50$).

The Gösgen experiment measured the $\overline{\nu}_e$ spectrum at three distances up to 64.7 m from the reactor by using the inverse beta decay reaction $\overline{\nu}_e + p \rightarrow e^+ + n$. The reactor had a thermal power of 2800 MW, while the detector

EXPERIMENT	NEUTRINO TARGET MASS	REACTOR DISTANCE (max.)	Δm^2 (90% c.l.) (min.)	REF.
Grenoble	320 kg	8.75 m	.15	[21]
Savannah River	260 kg	24 m	.05	[22]
Gösgen	320 kg	65 m	.019	[23]
Krasnoyarsk	600 kg	92 m	.014*	[24]
Rovno	200 kg	25 m	.06	[25]
Krasnoyarsk	600 kg	200 m	.01	[26]
Bugey III	1200 kg	40 m	in progress	[27]
San Onofre	12000 kg	700 m	2×10^{-3}	[28]
Chooz	4800 kg	1025 m	1×10^{-3}	this proposal
Perry	1000 ton	12.9 km	1×10^{-4}	[29]
			*68% c.l.	

Table 2.1: Summary of reactor neutrino oscillation experiments. The last three experiments listed are current or future proposals.

provided a target mass of 320 kg and yielded a neutron detection efficiency of 21.7%.

The results of the Gösgen experiment as well as several other reactor neutrino oscillation experiments are summarized on the exclusion plot shown in Fig. 2.4. In this plot, for example, the area above and to the right of the curve labelled "Gösgen" is the region of the Δm^2 vs. $\sin^2 2\theta$ phase space where neutrino oscillations would have been detected by this experiment had they been present. The minimum detectable Δm^2 for maximal mixing was $1.9 \times 10^{-2}\,\mathrm{eV}^2$.

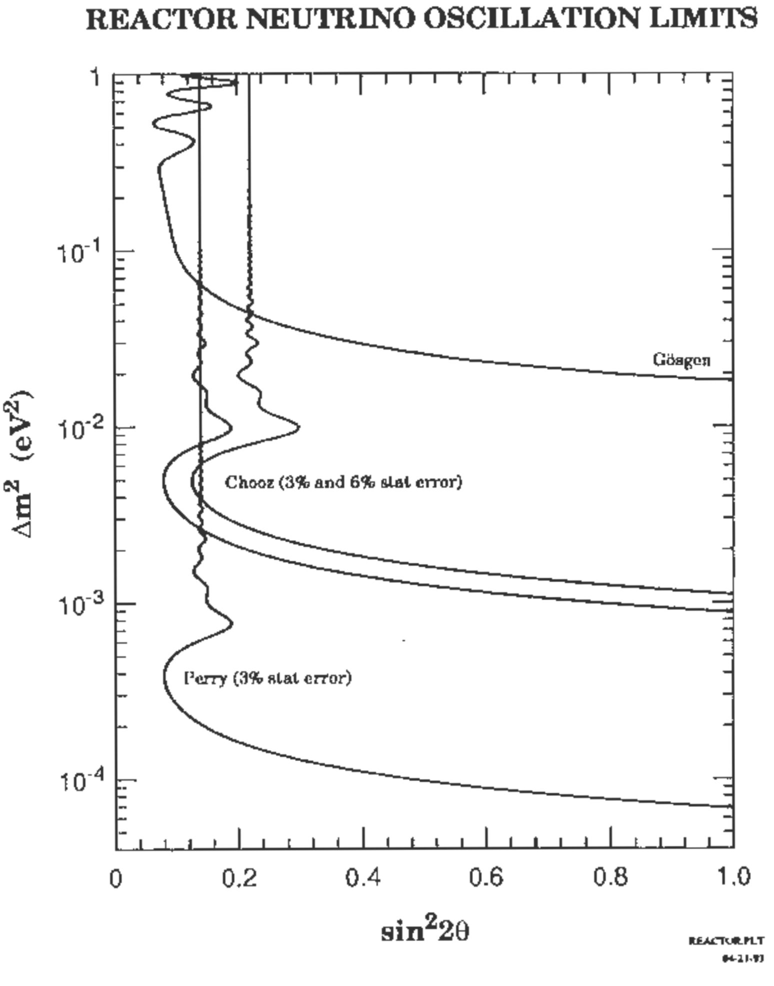

Figure 2.4: Reactor neutrino oscillation limits showing 90% c.l. exclusion contours. The Chooz experiment will extend existing results by more than one order of magnitude in Δm^2. The future Perry experiment would allow an additional ten-fold sensitivity improvement.

Chapter 3

Description of the Experiment

We are proposing the Chooz experiment as a highly sensitive neutrino oscillation search using an underground facility near a nuclear power station. We believe this experiment is the next logical step in the systematic exploration of the neutrino oscillation parameter space. Additional motivation is provided by the unexplained anomalies observed in solar and atmospheric neutrino measurements.

The experiment will look for the spectral distortion and flux reduction which would signal the existence of vacuum oscillations of the electron antineutrino beam emitted by the twin power reactors. The limits on neutrino oscillations expected are shown in Fig. 2.4 by the curves labelled "Chooz". For maximal mixing, the experiment would detect oscillations for values of $\Delta m^2 > 1 \times 10^{-3}\,\mathrm{eV}^2$, an order-of-magnitude improvement over currently available limits. The experiment would also provide an excellent testing ground for methodology for the future Perry experiment (see Table 2.1 and ref. [29]). An overview of the Chooz experiment is shown in Fig. 3.1.

3.1 Neutrino Source and Site

The neutrino source is a pair of reactors at the Chooz B nuclear power station in the Ardennes region of northeastern France. Each of the PWR reactors will have a thermal power of 4.2 GW and is scheduled for startup by the end of 1995. An essential feature of the experimental site is the availability of a tunnel with an overburden of 115 m of rock, equivalent to 300 m of water. Building the neutrino detector in this tunnel will provide the cosmic-ray shielding needed to preserve the signal/noise ratio against a one hundred-fold neutrino flux reduction with respect to previous experiments. The advantages of such a site are made clear by Fig. 3.2

3.2 The Detector

The neutrino detector is shown in Fig. 3.3, while its principal design parameters are exhibited in Fig. 3.4. The neutrino target will be contained in a 5.5-m-diameter cylindrical steel tank shielded locally by about 75 cm of low radioactivity material. The tank will contain three concentric liquid scintillation detectors: an outer 90-ton veto counter; an intermediate 17-ton optically separated event containment detector; and a central acrylic vessel containing five tons of a specially developed gadolinium-loaded liquid scintillator. The outer two vessels will contain a high flash point pure hydrocarbon scintillator also specially developed for this experiment.

Scintillation photons from particle interactions in the two inner detectors will be collected by 160 eight-inch photomultiplier tubes and processed by fast multi-hit ADC/TDC's and fast waveform digitizers. The detector will have good energy resolution, with about 76 photoelectrons detected per MeV of ionization energy deposited.

In the veto counter, light will be collected by 40 PMT's which can be installed either on the same structure as the 160 target-viewing PMT's or on the top and bottom parts of the main tank. The first of these options would provide a 50% larger photoelectron yield, but would require the use of more expensive PMT's.

Primary shielding against background will be provided by the 300 mwe-thick rock overburden, which will reduce the surface cosmic ray muon flux by a factor of 300, as shown in Fig. 3.2. The residual cosmic ray background is further suppressed by the 90-ton outer veto counter, which also provides additional shielding against ambient radioactivity.

Neutrinos above the threshold energy of 1.8 MeV will be detected by the reaction $\overline{\nu}_e + p \rightarrow e^+ + n$. The observable energy from this reaction will equal the positron kinetic energy augmented by 1.022 MeV resulting from detection of the positron annihilation gamma rays. Following thermalization of the recoil neutron, an additional 8 MeV will be detected as a result of capture of the neutron by a gadolinium nucleus (time constant $28\,\mu s$). Thus, a readily recognizable delayed coincidence pulse pair will signal the neutrino interaction. The 8 MeV neutron capture event will be well separated from the beta and gamma radiation accompanying decay of members of the ubiquitous uranium and thorium decay chains and from the decay of ^{40}K. Further significant rejection of the accidental coincidence background will be possible by software reconstruction of the positron and neutron capture vertices to which would be applied a cut requiring spatial separation not to exceed 1.5 m.

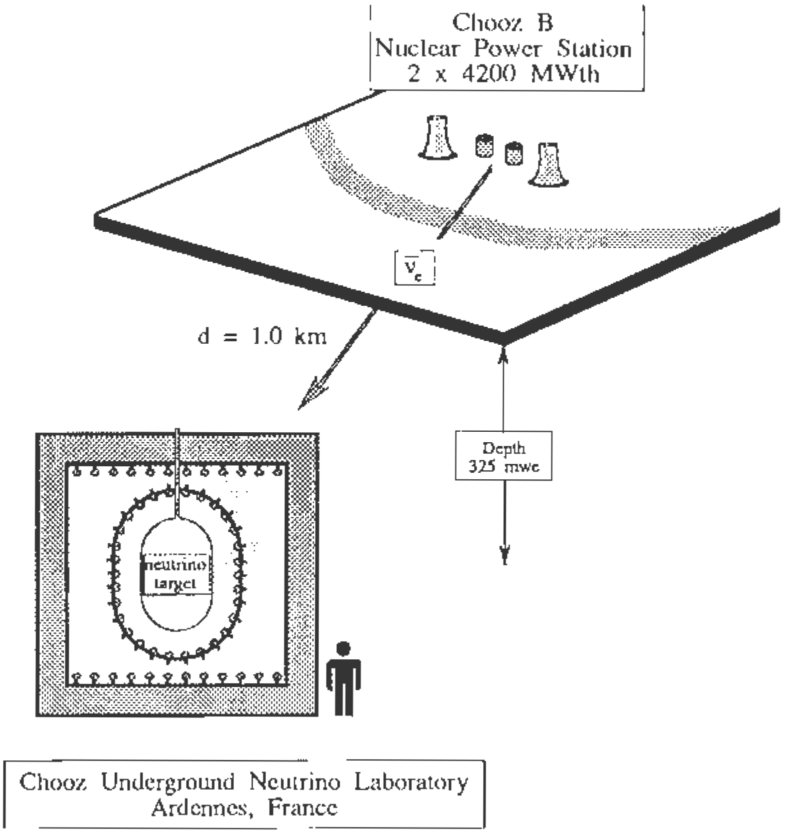

Figure 3.1: Overview of the experiment. Detection of the weak neutrino signal at 1 km is made possible by the 300 meter of water equivalent shielding above the detector, which attenuates the otherwise overwhelming cosmic ray muon-induced background by a factor of 300 and by the layered design of the detector and its local shielding. The high detection efficiency for antineutrino events (more than 80%) further enhances the expected signal-to-background ratio and facilitates accurate determination of the detector efficiency, needed for accurate comparison of the measured and expected neutrino fluxes.

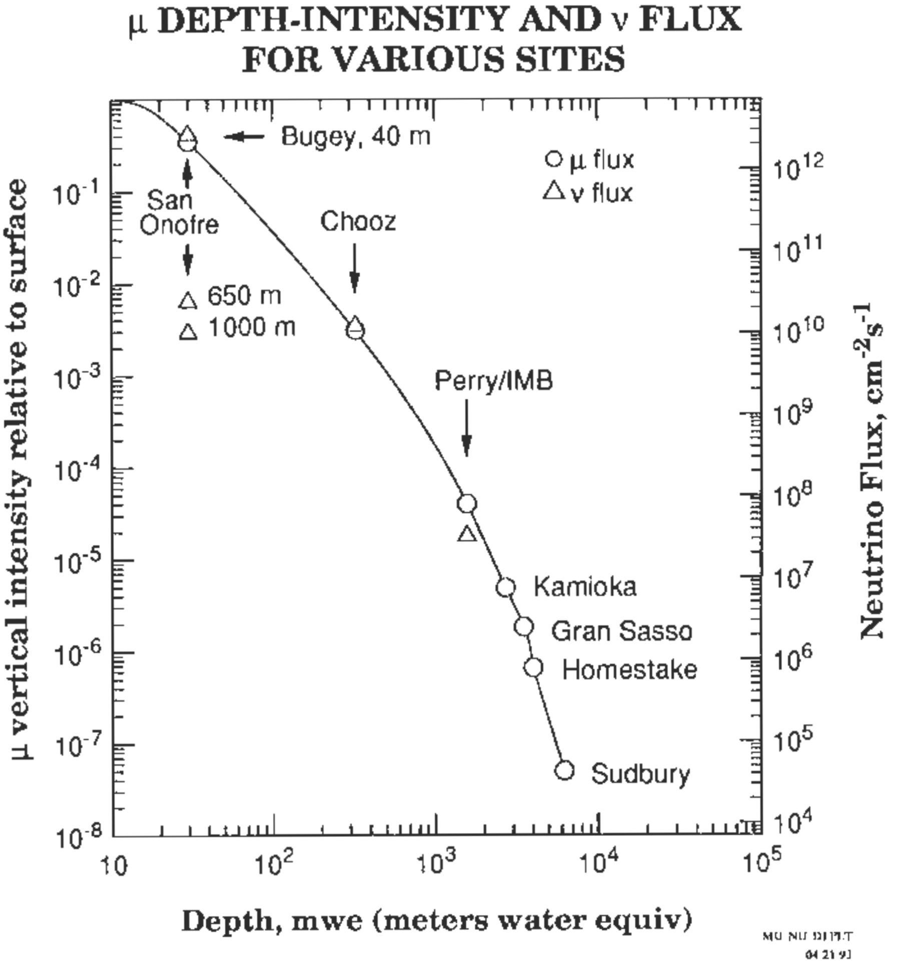

Figure 3.2: Muon depth vs. intensity and neutrino flux at various sites. At Chooz (and to a somewhat lesser extent at Perry/IMB) the low neutrino fluxes available for long baseline oscillation experiments are compensated by comparably reduced muon fluxes. Since cosmic ray muons produce the most serious backgrounds in these experiments, shallow sites such as that at San Onofre are at a serious disadvantage.

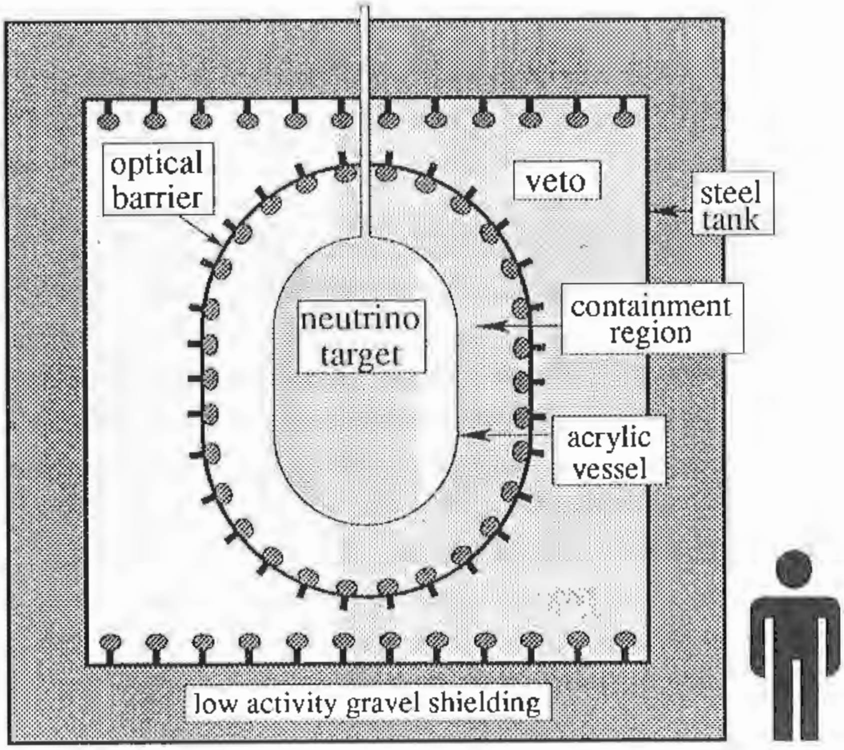

Figure 3.3: The Chooz detector. The neutrino target contains 4.9 tons of gadolinium-loaded liquid scintillator in which the reaction $\overline{\nu}_e + p \rightarrow e^+ + n$takes place. The positrons and their annihilation photons are detected at zero time delay, while the neutron is detected typically between 10 and 100 μs later following thermalization and capture by a gadolinium nucleus, leading to the release of a total of about 8 MeV of γ rays. A 300 meter of water equivalent underground location and massive gravel, steel and liquid scintillator shielding suppress the background to a few counts per day, about 10 times lower than the anticipated neutrino event rate.

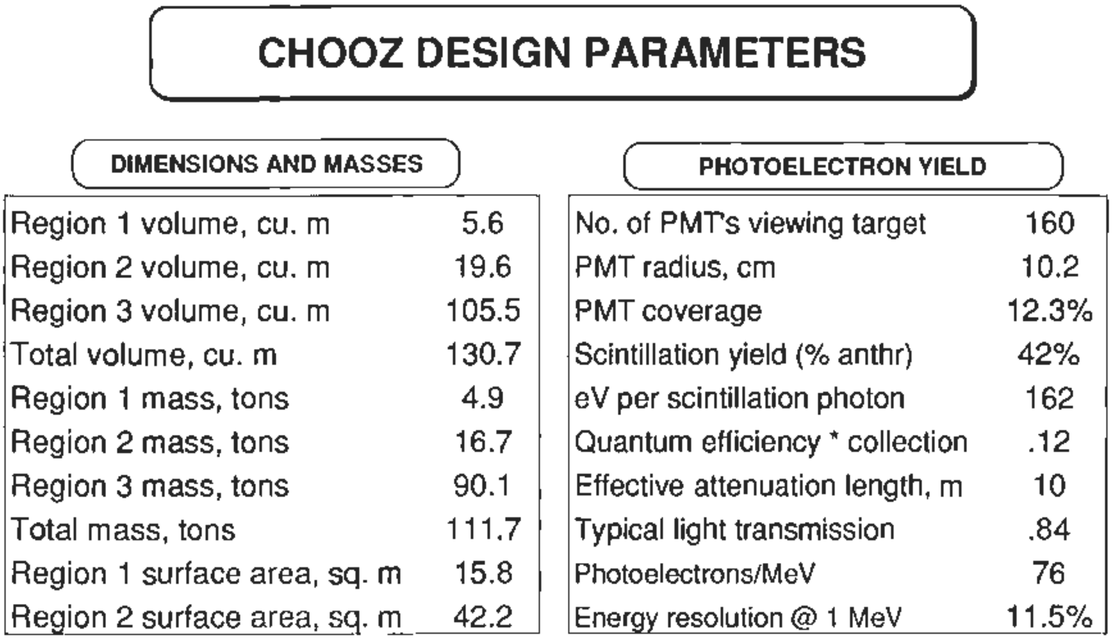

CHOOZ DESIGN PARAMETERS

DIMENSIONS AND MASSES	
Region 1 volume, cu. m	5.6
Region 2 volume, cu. m	19.6
Region 3 volume, cu. m	105.5
Total volume, cu. m	130.7
Region 1 mass, tons	4.9
Region 2 mass, tons	16.7
Region 3 mass, tons	90.1
Total mass, tons	111.7
Region 1 surface area, sq. m	15.8
Region 2 surface area, sq. m	42.2

PHOTOELECTRON YIELD	
No. of PMT's viewing target	160
PMT radius, cm	10.2
PMT coverage	12.3%
Scintillation yield (% anthr)	42%
eV per scintillation photon	162
Quantum efficiency * collection	.12
Effective attenuation length, m	10
Typical light transmission	.84
Photoelectrons/MeV	76
Energy resolution @ 1 MeV	11.5%

chdespar xls
29-Apr-93

Figure 3.4: Design parameters of the detector.

We anticipate a total running time of two years will be adequate to achieve our goal of a statistical error better than 4%. Neutrino oscillations would be uncovered by comparing the observed integral count rate with an accurately calibrated detector-efficiency Monte Carlo calculation. Information on reactor power and fuel burn-up will be available from the power station. The neutrino flux per unit power will be determined from calculations which currently are reliable to about 2%, especially at low energy, where a neutrino oscillation signal would probably be strongest. In the event of a positive signal, it would be useful to construct a close-in detector to provide a flux independent confirmation. A detector site at less than 100 m from the reactors is available if needed.

Chapter 4

Details of the Experiment

4.1 The Neutrino Source

4.1.1 The Chooz Reactors

The neutrino source for the experiment will be a pair of reactors which are in the final stages of construction at the Chooz B nuclear power station of the French national utility company Electricité de France (EdF). The pressurized light water reactors (PWR's), located in the Ardennes region of northeastern France, will each have a thermal power of 4.2 GW and are both scheduled for startup by the end of 1995.

The main fissile material in the Chooz PWR's is ^{235}U, which undergoes thermal neutron fission. The fuel is enriched to about 3.5 % in the ^{235}U isotope. Fast fission neutrons are moderated by light water pressurized to 150 bar. The dominant natural uranium isotope, ^{238}U, is fissile for fast neutrons (threshold 0.8 MeV) and generates fissile ^{239}Pu by thermal neutron capture –

$$n + {}^{238}\mathrm{U} \rightarrow {}^{239}\mathrm{U} \rightarrow {}^{239}\mathrm{Np} \rightarrow {}^{239}\mathrm{Pu}\ (\mathrm{T}_{1/2} = 24,100\,\mathrm{y})\ .$$

The isotope ^{241}Pu is produced in a similar manner from the ^{239}Pu –

$$n + {}^{239}\mathrm{Pu} \rightarrow {}^{240}\mathrm{Pu} + n \rightarrow {}^{241}\mathrm{Pu}\ (\mathrm{T}_{1/2} = 14\,\mathrm{y})\ .$$

For each fission, the mean energy release is ~ 204 MeV, and the average number of $\overline{\nu}_e$ is ~ 6. Therefore, at full power for the two Chooz reactors (8.2 GW), the rate of neutrino production can be estimated to be

$$R_\nu = \frac{6 \times P_{th}}{204\,\mathrm{MeV}} = \frac{6 \times 8.2 \times 10^{9} \times 6.24 \times 10^{12}}{204}$$

	Start of Cycle	End of Cycle
^{235}U	60.5 %	45.0 %
^{238}U	7.7 %	8.3 %
^{239}Pu	27.2 %	38.8 %
^{241}Pu	4.6 %	7.9 %

Table 4.1: Fraction of fissions from the four fissile materials (cycle 11 of Bugey reactor 5).

$$= \quad 1.5 \times 10^{21}\,\bar{\nu}_e\,\mathrm{s}^{-1}.$$

As the reactor operates, the concentration of ^{235}U decreases, while those of ^{239}Pu and ^{241}Pu increase. After about one year, the reactor is stopped and 1/3 of the fuel elements are changed. Typical numbers for an annual cycle are given in Table 4.1.

4.1.2 Monitoring the Neutrino Rate

Thermal Power of the Reactor

In previous reactor neutrino experiments at Bugey, the thermal output was obtained from measurements on the secondary water loop, where the temperature difference is larger than on the primary one (typically 270° C vs. 219° C). The error on this parameter is ≤ 1 %. Measurements were available every 10 minutes over a computer network. The data were cross-checked with continuous neutron flux measurements around the reactor vessel. This error includes the error on small corrections (about 11 $\mathrm{MW_{th}}$) due to power for the primary pumps, *etc.*

Changes of the Fuel

The unit used to describe the nuclear fuel evolution is the MW day/ton, which measures the amount of energy per ton extracted from the nuclear fuel since its first entry in the reactor core. This quantity is called β, the "burnup".

The core of each Chooz reactor will contain 205 nuclear fuel elements, 1/3 of which will be changed each cycle. The new nuclear fuel elements are installed in the outer part of the core. Burnup data for each element will be provided by the utility company at the start and end of each cycle. For the start-up of the reactors, all fuel elements will be brand-new with $\beta = 0$. To simulate partially used nuclear fuel, 1/3 of the core will be less enriched and 1/3 will have a very low enrichment:

69 elements at 1.8 %
68 elements at 2.4 %

^{235}U	201.7 ± 0.6
^{238}U	205.0 ± 0.9
^{239}Pu	210.0 ± 0.9
^{241}Pu	212.4 ± 1.0

Table 4.2: Energy release per fission, in MeV.

68 elements at 3.1 % .

The fuel enrichment for the following cycles is not yet entirely defined, but should be ~ 3.5 %.

Knowing the burnup of each element at the beginning and end of each cycle, as well as the total daily burnup, we can compute the daily burnup of each element. These values are then used to obtain the day-to-day amount of each fissile element in the reactor using a table which exists for each initial ^{235}U enrichment.

Since the energy release per fission from each fissile element is known (Table 4.2), we can compute the mean energy released per fission each day. The number of fissions is then obtained by dividing the thermal power by this number.

4.1.3 Neutrinos From Each Fissile Element

Among the four fissile materials, three (^{235}U, ^{239}Pu and ^{241}Pu) undergo thermal neutron fission, while ^{238}U is fissioned by fast neutrons.

The neutrino rate per fission has been measured for the first three isotopes by Borovoi *et al.* [39] and by Schreckenbach *et al.* [40] -[43]. The latter measurement includes the shape of the energy spectrum and has an accuracy of 2 % from point to point and an overall normalization error of 2.8 %. The normalization error is the most important in our case, since we want to measure the total number of neutrinos at 1 km from the source. The point-to-point error, which will be used to determine the effect of the positron threshold, is also known from high statistics measurements such as those at Rovno [44] or Bugey 3 [45].

The Schreckenbach measurement can be compared to several computations and is found to be in good agreement with that of Klapdor and Metzinger [46]. We will therefore use this computation for the ^{238}U neutrino rate, which has not been measured. The ^{238}U contribution to the total number of fissions is ≤ 10 %, and is therefore not a major source of error.

4.1.4 Direct Neutrino Measurements

A very precise measurement of the total number of neutrinos has been published by the Rovno group [47]. Their detector measures the integral number of neutrino interactions by detecting only the neutron from the inverse beta decay reaction, thereby avoiding positron threshold corrections and most of the analysis cuts needed for the correlated positron-neutron selection. The target is pure water, and the neutron is detected in ^{3}He proportional counters in the water. The published error on this measurement is 2.8 %.

The same detector is now running at 15 m from the Bugey reactor, with new electronics, to evaluate some of the systematic errors of the Bugey neutrino program. This measurement is being performed by three laboratories of the Chooz collaboration (Moscow, Paris and Annecy) and will be useful for knowledge of the Chooz reactor neutrino flux, with an overall uncertainty ≤ 3 %. Since the Bugey and Chooz reactors are both pressurized water reactors, measurements can be scaled from one reactor to the other with small systematic errors.

4.2 Detector Mechanical Design

The Chooz detector consists of a vertical cylindrical steel tank containing three scintillating volumes (see Fig. 3.3). A transparent acrylic inner vessel (Region 1) contains the gadolinium-loaded liquid scintillator neutrino target. Regions 2 and 3 are filled with an unloaded high flash point hydrocarbon liquid scintillator. Separating Regions 2 and 3 is a structure (the "geode") to support the photomultiplier tubes. The geode allows free passage of liquid, but is opaque to allow the use of Region 3 as a cosmic-ray tagging detector.

160 PMT's will collect light from the inner vessel, while 41 more will be mounted on the geode facing outward toward the veto region. (A possible design option is to mount the veto PMT's on the top and bottom of the steel tank, as shown in Fig. 3.3). The inner and outer surfaces of Region 3 will be coated with a white diffusing paint to optimize light collection in the veto. Inside the geode, black paint will be used to improve the event localization performance of the detector by reducing reflections.

4.2.1 Target

The inner vessel is made of two hemispheres joined by a cylinder the outer dimensions of which are 1.8 m diameter and 2.8 m high. The inner volume is 5.6 m^3, while the mass is 150 kg (empty).

The vessel is fabricated from the thermoplastic polymer polymethylmethacrylate (commercial name – Altuglass) which has excellent optical and mechanical properties and resistance to the chemicals of the liquid scintillators. Each hemisphere is formed without the use of expensive molds by a blowing process consisting of pressurizing the gap between a hot acrylic sheet and a flat metal surface to which the sheet is firmly attached. The size of the acrylic sheets is 2 × 3 m, leading to a hemisphere diameter of 1.8 m. After blowing and machine finishing, each hemisphere is flanged.

The cylindrical part of the target is formed by bending 8 mm-thick flat acrylic sheets into half-cylinders. After the two half-cylinders are joined, two flanges and five longitudinal stiffening plates are glued on. Final assembly of the hemispheres on the cylinder is then made by gluing together the flanges. The five longitudinal plates are used to support the target on acrylic pillars and to attach it to the geode. The upper part of the target is fitted with a 70 mm-diameter flange to allow passage of filler pipes, calibration sources and various sensors.

4.2.2 PMT Support Structure – the "Geode"

The geode has the same general shape as that of the target - a cylinder with hemispherical endcaps. The outer dimensions are 3.2 m diameter and 4.2 m high. The surface area is $42\,\mathrm{m}^2$ and the total weight 1150 kg. The PMT's are mounted on this structure, the mean distance between optical centers being ~ 50 cm. The total number of PMT's is 201 – 160 looking toward the target, and 41 in the opposite direction, toward the veto.

The geometry of the geode consists of two semi-icosahedra enclosing the ends of a cylinder. A PMT support flange is placed at each of the 12 vertices of the icosahedron. Three additional PMT's are mounted along each of the 30 edges of the icosahedron, together with three more mounted on each of the 20 faces, for a total of $12 + 90 + 60 = 162$ PMT's mounted on the icosahedral structures. The cylindrical part of the geode adds 40 more PMT's. Since the apex PMT position is left empty for passage of the neck of the inner vessel, the total number of usable PMT positions is 201.

All PMT support flanges are linked by a system of rods. The flanges, rods, and the optical screens are made either of stainless steel or painted carbon steel. The flanges have an L-section of $30\times30\times3$ mm, the rods a T-section of $30\times30\times3$ mm, while the thickness of the screens is 0.5 mm.

The geode is built by welding the upper hemisphere and the cylinder onto the lower hemisphere with the help of an assembly jig. On the lower part of the geode will be added five nodes to support the acrylic vessel on one side, and, on the other, to place the geode onto its main support pillars which, in turn, are attached to the floor of the main tank. On the upper part of the geode, additional nodes will be created to attach handling bars and for 15 ropes to support the PMT cables.

4.2.3 PMT Mounting

The PMT mounts allow orientation of the tubes either inward or outward. Each mount consists of two flanges and a cap made of pressed steel. The back flange has a zigzag barrier for light tightness, and the tube cap has the same aim.

4.2.4 The Main Tank

The main tank is a vertical steel cylinder with endcaps. The outer dimensions are 5.5 m diameter and 6.2 m high. The lower endcap has a depth 0.56 m, with a 7 m radius of curvature.

The volume is 141 m^3, and the empty weight is 9.9 tons. The cylindrical section of the tank will be 8 mm thick, while the endcaps will be 12 mm thick. Due to the limited working space in the tunnel, all pieces of the main tank will be prepared in the factory and welded inside the tunnel or in the experimental hall. The assembly of the cover to the body of the main vessel is made with bolted flanges (75×25 mm in cross section) which are sealed with a teflon gasket.

High voltage and signal feed-throughs use 36 flanges equipped with glass-to-metal coaxial insulators welded to the tank side near the top.

All inner and outer surfaces will be mechanically prepared and polished before primer is applied followed by the finishing coats.

4.3 Experimental Facilities

The detector chamber will be located about 135 m from the entrance to the tunnel known as the "galerie de marinage", with an overburden of 115 m of rock. The chamber will have 4.6 m of head space above the top of the detector and will be 24.1 m long and 7.1 m wide at the detector. The chamber will be dehumidified and maintained at a temperature of 18-24°C. Near the detector chamber there will be an electronics hut.

Outside the tunnel, an auxiliary hall is planned, with small electronics and machine shops, a control room for the experiment, and storage tanks and mixing areas for the liquid scintillator. Pumps and plumbing lines will be installed between this area and the detector. Filling of the inner target vessel and of the main tank will be done simultaneously to reduce pressure differentials on the acrylic chamber. Inert gas blanketing will be provided both to protect the scintillator from oxidation and to enhance its light output.

For many additional details, see Ref. [48].

4.4 Photomultiplier Tubes

Photomultipliers in the Chooz experiment provide time and pulse height information, which is used to determine the energy deposited and its location. The geometry of the detector, a central volume of scintillator surrounded by photomultipliers (PMT's) is common to the Borexino [30], LSND [31] and SNO [32] detectors. These detectors utilize timing and pulse height information in a manner similar to the Chooz detector.

Communications with members of these experiments and related documents have been very helpful, allowing us to select PMT's and preparation techniques

PARAMETER	Burle	Hamamatsu	Philips	EMI	unit
photocathode area	434	283	366	366	cm^2
1 pe time jitter	1.0	1.4	0.9	1.0	ns
after-pulses	7.6	5.0	24.2	1.3	%
1 pe pulse ht. res.	37.5	75.0	57.2	39.4	%
peak/valley	3.4	1.3	1.7	2.8	
dark rate	5000	3500	1300	650	Hz
B @ 80% pulse ht.	150	550	$\geq$ 600	300	mG
mass	4400	900	1000	700	g
thorium	NA	40	NA	100	ppb
uranium	NA	40	NA	70	ppb
potassium (nat.)	NA	30	NA	150	ppm

Table 4.3: Properties of photomultipliers.

appropriate for Chooz without repeating the extensive tests performed by the other groups.

The EMI 9351 PMT, an upgraded version of the 9350 used in MACRO, seems to be best for our needs, while the base and potting technique used for SNO are preferred. Light flashers and data acquisition methods can be copied directly from LSND for the PMT testing. Compromises on these choices can be made for reasons of cost, availability or other reasons without seriously affecting the quality of our experiment at Chooz. Comments on alternatives will be made in the individual sections below.

4.4.1 Selection

The categories of interest for tube selection are performance, radioactivity and cost. The Hamamatsu 4558, EMI 9351, Philips XP1802 and Burle C83061E photomultipliers are large area, fast timing PMT's which can detect single photoelectrons. The Borexino proposal [30] includes an exhaustive study of their characteristics, which we have supplemented by information from LSND and SNO (Hamamatsu PMT's). The performances are summarized in Table 4.3.

The Burle PMT has high sensitivity to magnetic fields, which would require care and expense to shield, and also has a large mass and volume, which increase radioactivity and the problems of mounting it submerged in scintillator. The Philips PMT has after-pulsing 24% of the time, which would reduce its effectiveness for pulse shape discrimination of electrons, protons and alphas. The other

ITEM	^{208}Tl	U	^{40}K
EMI 9351 (low act.)	.036 Hz	.122 Hz	4.84 Hz
SNO base	.0025 Hz	.011 Hz	.0035 Hz
Ham. 1408 (4558)	.021 Hz	.105 Hz	1.45 Hz
LSND base	.027 Hz	.012 Hz	.02 Hz

Table 4.4: Count rate in target due to PMT radioactivity.

two PMT's are adequate for our needs, the EMI being superior in resolution and dark rate, but somewhat sensitive to magnetic fields when the dynodes are parallel to the field direction.

Radioactivity in the PMT and its base must not create significant numbers of "fake" events. Neutrons captured on Gd (.01 Hz, a conservative estimate) and a gamma ray from natural radioactivity can form an accidental coincidence that fakes the positron-neutron delayed coincidence signal of the experiment. If the gamma rate is 10 Hz (estimated upper limit) and the coincidence time is taken to be 64 μs, then the accidental rate becomes $.01 \times 10 \times 64 \times 10^{-6}\,\mathrm{s}^{-1}=0.6\,\mathrm{d}^{-1}$ in the target (region 1).

This rate is acceptably small compared to the event rate of about 30 d^{-1}. As a crude standard, we require the PMT radioactivity to make less than a 10 Hz count rate in the target. Using the PMT radioactivities in Table 4.3 and K, U and Th contaminations [33], [34], [35] in materials used for the PMT bases, we have calculated the total activity of an EMI 9351 with a SNO base, and of a Hamamatsu 1408 (same as the 4558 but with the low activity glass used in SNO and LSND) with an LSND base. The location of the PMT and base is about one meter from the target, giving an attenuation factor of about 100 and a solid angle factor of about 1/15 for the actual count rate. Table 4.4 shows the count rate in the target due to gamma rays from the 160 PMT's and bases.

All count rates are lower than our nominal goal of 10 Hz, even assuming a trigger threshold of about 1 MeV, which is lower than necessary. If we were to operate with a threshold of 1.5 MeV, eliminating the ^{40}K counts, the fake positrons would be 100x down from our 10 Hz goal. We conclude that either of the two bases and PMT's are adequate. Note that this would not be the case without placing the PMT's one meter from the target.

The cost of the photomultipliers has not been determined by competitive bids, but is expected to be near $900 per PMT, based on an estimate from EMI. Price and availability may be the deciding factors between EMI and Hamamatsu.

4.4.2 Testing

The photomultipliers will be tested to see that they have the necessary resolution for the timing and pulse height of single photoelectrons and the high voltage needed to achieve a standard gain will be determined. The dark noise rate at this voltage will be measured after a stabilization period of about a day.

The peak-to-valley ratio of the single photoelectron (1 pe) pulse height spectrum should be at least 1.1 to enable the gain to be monitored by locating the peak of the spectrum. The dark noise rate at a gain of 10^7 should be less than 3 kHz, and the 1 pe timing resolution should be 4 ns FWHM (σ = 1.6 ns) or better.

A test setup with light pulsers and computer data collection will be used which is similar to that used for the LSND photomultiplier testing.

4.4.3 Preparation

Preparation consists of mounting a base on the PMT, testing the performance, and sealing the base against leaks before it is submerged in the detector. The final choice of the PMT (EMI or Hamamatsu) and the base have not been made.

The bases could be similar to those of LSND or SNO and still be adequate for our needs. They will have low current (0.1 ma) resistor strings and run on positive high voltage. The PMT's will have wire pins which will be directly soldered to boards containing the resistors and capacitors. LSND bases are rigid and can support a cable which is soldered to the board before dipping the assembly into a conformal coating made by Hysol. SNO bases are flexible, with a polypropylene cup around them which is filled with a sealing gel made by General Electric. The cable has a leakproof connector which screws onto a bulkhead connector on the cup. The former process is simpler, while the latter uses less hazardous (to humans) potting material, and is more convenient when mounting and connecting the PMT's. Tests are underway to see if there are incompatibilities between the scintillator and the potting compounds which would not have shown up in the SNO or LSND tests.

The sequence for testing will take 24 hours, and will involve the following:

1. Unpack PMT and attach the base.
2. Connect to high voltage and leave overnight.
3. Perform tests.
4. Seal the PMT if the tests are passed.
5. Allow the sealant to cure.

We expect to do about five PMT's each day.

ITEM	COST
Photomultipliers (160 @ $900, est'd)	$144,000
Bases (160 @ $40 for parts and potting)	6,400
Light flasher and dark box (5 @ $140)	700
Programmable pulser	3,000
Computer and interface card (Mac LCII)	2,000
Miscellaneous equipment (mainly for potting)	3,000
TOTAL	$159,100

Table 4.5: Estimated costs for photomultipliers.

4.4.4 Costs

Estimates of costs have been made by consulting Dave Works (LSND) and H. Mak (SNO) about their respective methods of base construction and potting. We have also assumed that our costs per PMT will be greater due to the smaller scale of the Chooz experiment. For data acquisition, the software and most of the CAMAC modules are available. We will buy a MacIntosh computer and interface card and a programmable pulser for the light flashers. Five dark boxes with light flashers will be constructed so that we can prepare five PMT's per day. Table 4.5 summarizes our expected costs.

4.4.5 Time Scale

According to discussions with the EMI representative, Mr. Avery, it would take about three months to fill an order for 160 PMT's, longer for more. If the first PMT's become available one month after the order, the preparation can proceed in parallel with the production at EMI and keep pace with it. If so, the PMT preparation can be finished four months after the order is placed.

Installation of PMT's into the detector could begin in January 1994 if the order is placed with EMI by September 1, 1993, assuming we test them all before starting to install them. However, it would be possible to start installation of the initially tested batches of tubes before receiving and testing the full order. In this case the order could be placed as late as November, 1993. We have not yet obtained comparable information for price and delivery dates from Hamamatsu.

4.5 Gd-Loaded and High Flash Point Scintillators

For the experiment, about 5 tons of Gd-loaded scintillator and 107 tons of high flash point hydrocarbon scintillator will be needed. Optimized formulations for each of these materials were developed after extensive testing at Drexel University. We thus have available for the experiment minimal cost yet high performance detection media. The properties of the two scintillators are listed in Table 4.6. Fig. 4.1 shows a recent remeasurement of the neutron capture time spectrum for a Gd-loaded scintillator sample mixed more than one year previously. The mean capture lifetime for this 0.05% Gd scintillator showed no change during this period, indicating satisfactory long-term stability of the material.

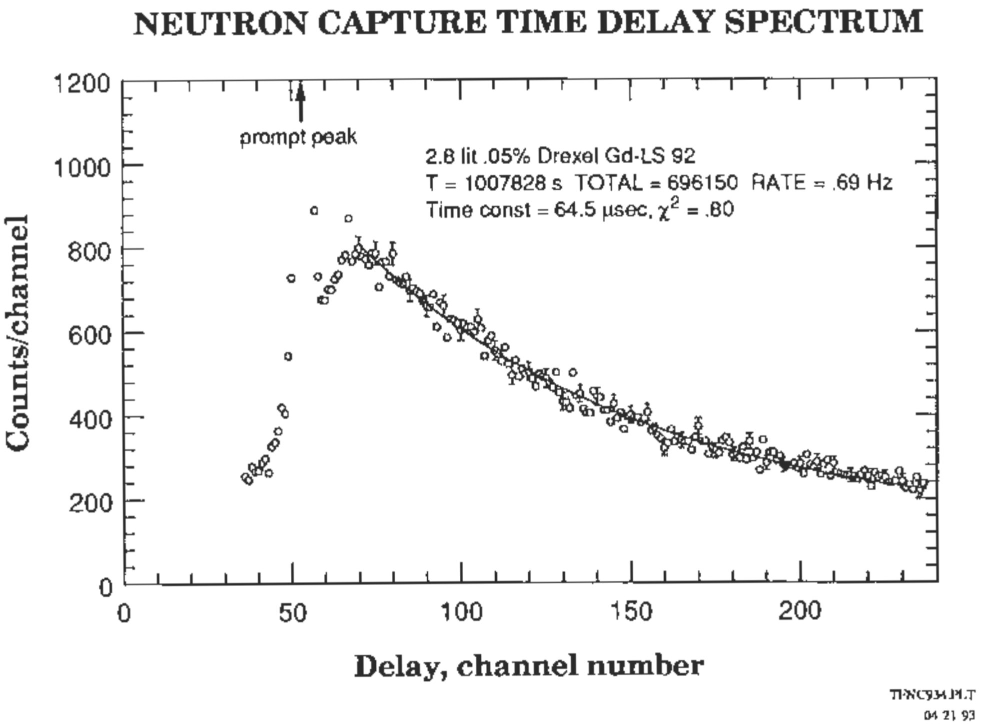

Figure 4.1: Neutron capture time delay spectrum with a 0.05% Gd-loaded scintillator. Thermal neutron capture events produce the exponentially decaying part of the curve between channels 70 and 236. A mean capture lifetime of $64\,\mu s$ is obtained by fitting an exponential plus constant term to this region. For the Chooz scintillator, a Gd concentration of 0.1% will thus yield a capture lifetime of about $30\,\mu s$. The prompt peak, indicated by the arrow, has been shifted by delaying the signal from the neutron channel. Prompt coincidences are caused both by cosmic ray showers and by scattered gamma rays from the Cm/Be neutron source.

	Gadolinium	**High Flash**
Chemical content:		
mineral oil	60%	97%
aromatics and alcohols	40%	3%
PPO, bis-MSB, etc.	0.2%	0.2%
Gd	0.1%	-
Compatibility	acrylic, ABS, PVC, CF4	acrylic, ABS, PVC, CF4
Density (@25°C)	0.869 gm cm^{-3}	0.854 gm cm^{-3}
Volume expansion coeff.	$7.9 \times 10^{-4}\mathrm{K}^{-1}$	$7.4 \times 10^{-4}\mathrm{K}^{-1}$
H/C ratio	1.93	2.02
Scintillation yield	42% of anthracene *-or-* 162 eV/photon	42% of anthracene *-or-* 162 eV/photon
Optical attenuation length	8 m	20 m
Flash point	69°C	110°C
Atomic composition:		
H	7.00×10^{22} atoms cm^{-3}	7.57×10^{22} atoms cm^{-3}
C	3.62×10^{22} atoms cm^{-3}	3.65×10^{22} atoms cm^{-3}
N	1.47×10^{19} atoms cm^{-3}	4.65×10^{18} atoms cm^{-3}
O	1.08×10^{21} atoms cm^{-3}	4.65×10^{18} atoms cm^{-3}
Gd	3.33×10^{18} atoms cm^{-3}	-
Neutron capture time	$27.6\,\mu s$	$180\,\mu s$
Gd capture fraction	86.7%	-
Thermal n mean free path	6.1 cm	39.7 cm

Table 4.6: Properties of the liquid scintillators developed at Drexel for use in the experiment.

Chapter 5

Electronics

5.1 Overview

The principal task of the electronics system for the Chooz experiment will be to provide a trigger when neutrino-like events occur, and to record timing and pulse height information from the PMT's for later event reconstruction.

The signals from each PMT will generally consist of only a small number of photoelectrons, with a timing spread characteristic of the transit time jitter of the PMT's (3.2 ns single p.e. FWHM for the EMI 9351).

The total amount of detected light from all of the PMT's is a good indication of the overall energy of the event, and the timing of the PMT pulses can give accurate event positions. Detailed timing and pulse-height information will be recorded by the electronics for offline event reconstruction.

The triggers for Chooz are primarily sensitive to energy deposition, based on the total number of detected photoelectrons and the total number of PMT's participating in an event. While the relative timing between PMT pulses contains useful information about the event location, this information is not used for triggering because the time differences are small. The transit time of scintillation light across the Chooz detector is 20 ns.

Figure 5.1 shows the overall scheme for one channel of the Chooz electronics. High-density commercial discriminators and TDC's will be used for the primary measurement of PMT pulse times, while waveform digitizers give both the PMT pulse heights and the multi-pulse detection needed to reject correlated background events.

5.2 Triggers

In Chooz, a simple Level 1 trigger system will be used to select events that have visible energy greater than a threshold of approximately 1 MeV. A delayed

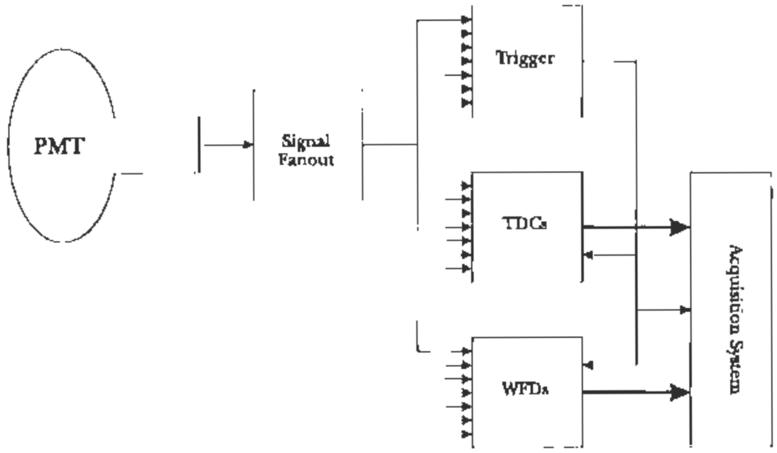

Figure 5.1: Overview of one channel of the electronics for Chooz. Commercial high-density TDC's will be used for pulse-timing, while waveform digitizers give pulse amplitude measurement and correlated background rejection

coincidence of Level 1 triggers generates a Level 2 trigger, which indicates a "neutrino-like" event, and causes readout of the acquisition electronics.

5.2.1 Level 1 Trigger

The Level 1 trigger for Chooz will be a fast, unbiased energy trigger. Since it is based only on the number of detected photoelectrons and the number of PMT's participating in an event, it will be easily calibrated and simulated, and its efficiency can be determined accurately.

Some Monte Carlo results illustrate the variations in detected photoelectrons and number of firing PMT's as a function of position in the detector. Figure 5.2 shows that the number of detected photoelectrons is a good measure of the total energy in the event, except when the event is in the outer 30 cm of Region 2, where the variations in total light yield are large because of the possibility that the event is near one PMT.

Events of a given energy in the outer part of Region 2 have fewer PMT's participating in the event (see Figure 5.3) than those closer to the center of the detector. This difference can be used to discriminate against events in the outer part of Region 2 that are near PMT's and therefore have an anomalously high number of total photoelectrons.

Chooz will use a Level 1 trigger based on both the total number of photoelectrons and the total number of PMT's in an event. Simple NIM electronics will generate a Level 1 trigger (see Figure 5.4) when both the number of PMT's firing is above threshold, and the total amount of light detected by the PMT's

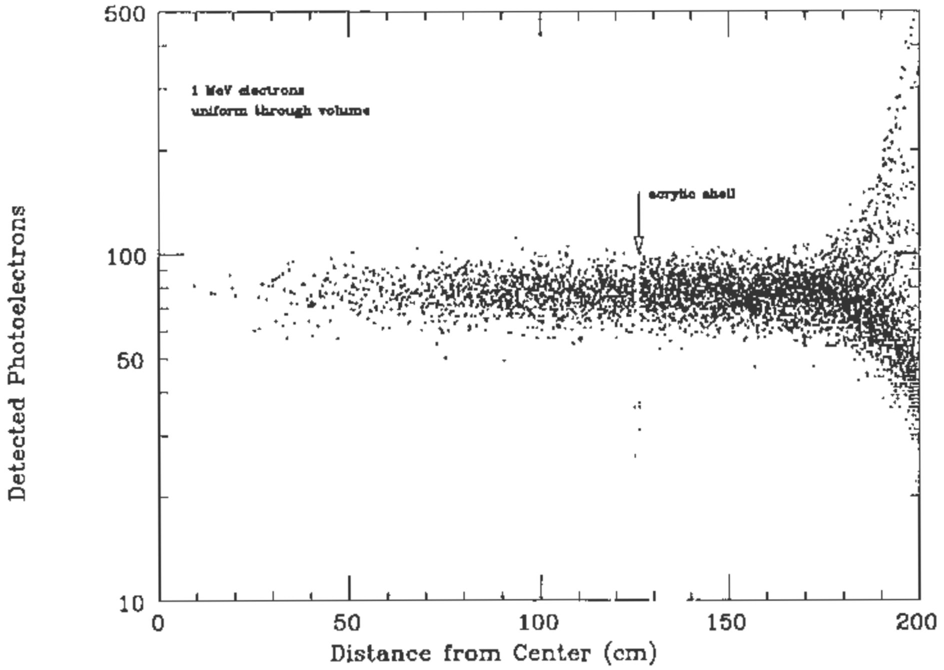

Figure 5.2: Number of photoelectrons for Monte-Carlo 1 MeV electrons in Chooz as a function of distance from the center of the detector.

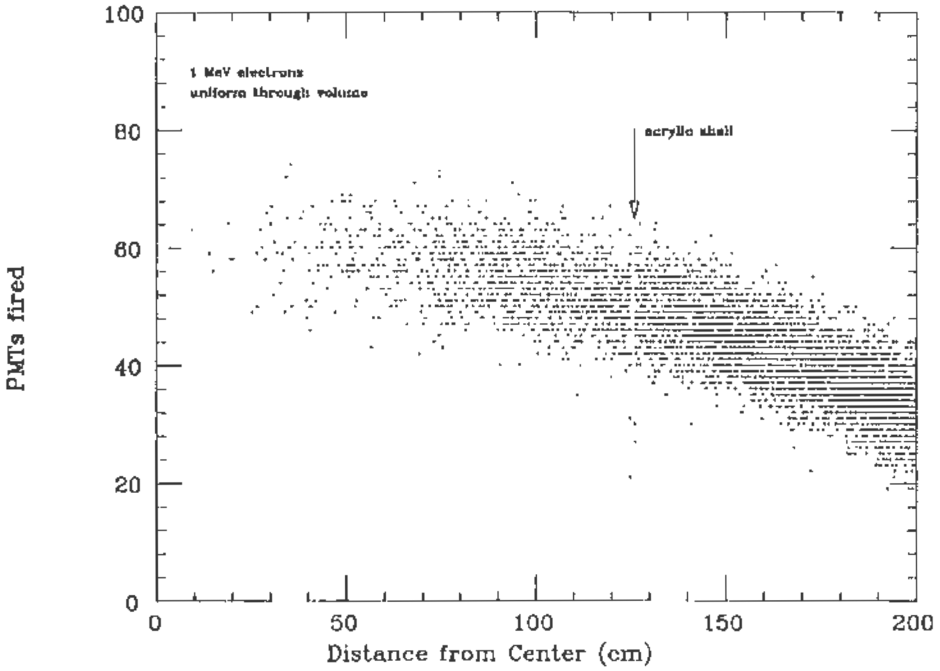

Figure 5.3: Number of PMT's that fire for Monte-Carlo 1 MeV electrons in Chooz as a function of distance from the center of the detector.

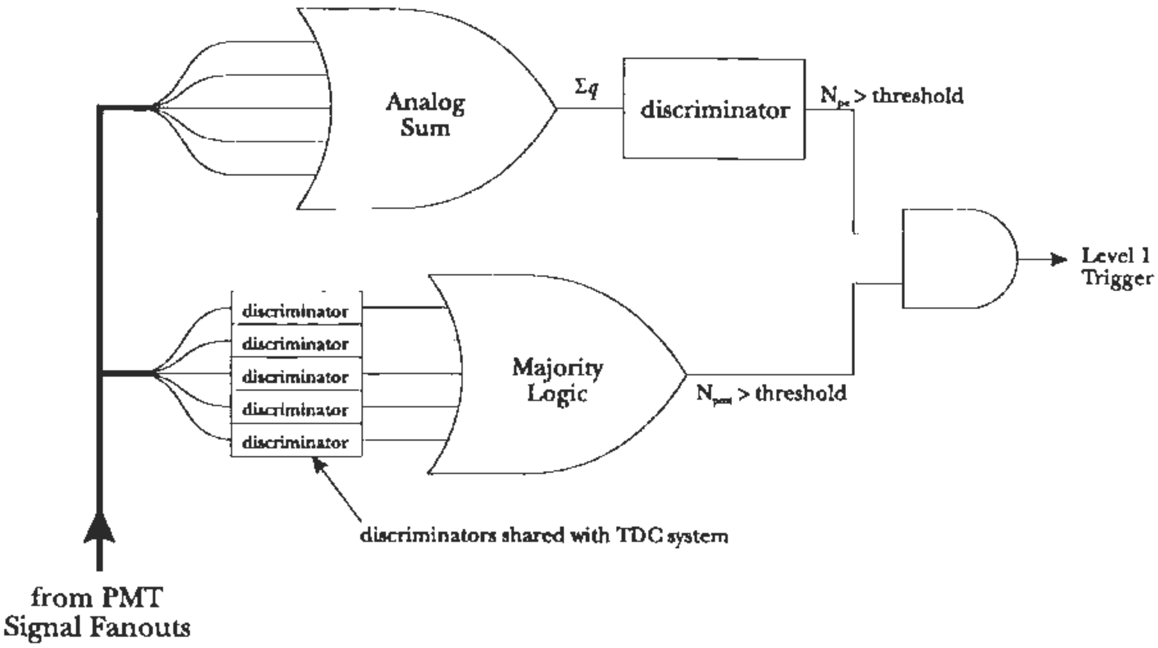

Figure 5.4: The Level 1 trigger for Chooz will require both the total photoelectron number and the number of PMT's fired to be above threshold, resulting in a simple, reliable and fast "energy deposition" trigger.

is above threshold.

The PMT signals will be linearly summed, using MACRO-type fanin modules developed at Drexel, to give the "total photoelectrons" signal. This signal is discriminated, giving an output pulse when the total number of photoelectrons in the event is above threshold.

The discriminators used in the TDC system have an output signal proportional to the number of channels firing; when these signals from the discriminators are linearly summed it gives the "total PMT's fired" signal, which will also be discriminated (as in majority logic) to give a signal when the number of PMT's firing is above threshold.

A coincidence of the "above photoelectron threshold" and the "above PMT's fired threshold" gives the Level 1 trigger. The Level 1 trigger is fast (approximately 100 ns), so long delays are not needed on TDC inputs, and should be robust, inexpensive and easy to implement.

The energy sensitivity of the Level 1 trigger scheme was checked using events generated by Monte Carlo. Figure 5.5 shows trigger efficiencies as a function of energy and distance from the center of Chooz for a trigger based only on detected photoelectrons. Figure 5.6 shows a similar set of efficiencies when a

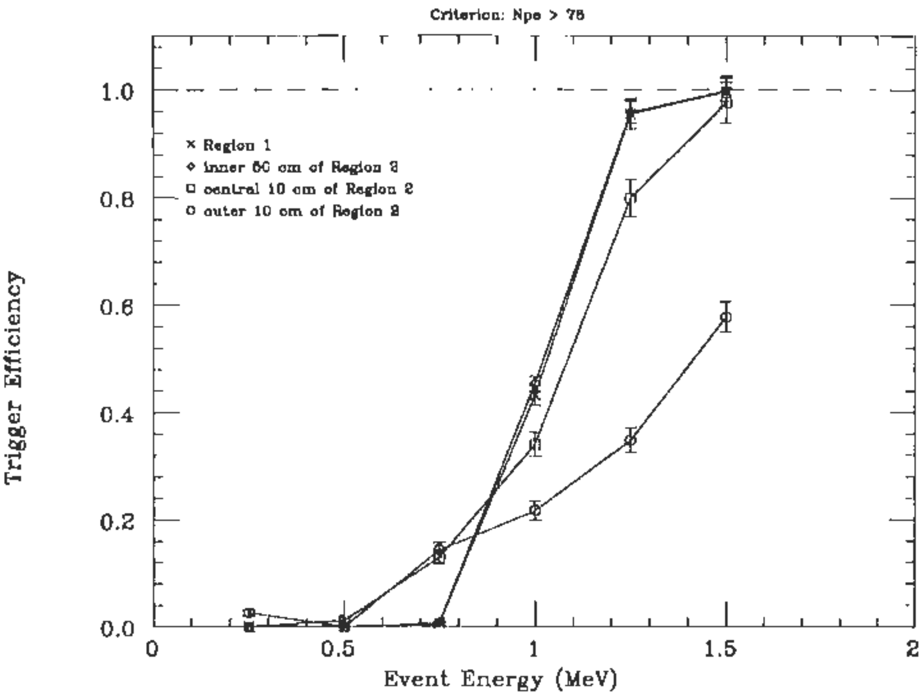

Figure 5.5: Efficiency as a function of energy shown for several regions of the Chooz detector, using a trigger criterion based only on the total number of detected photoelectrons. Low energy events in the outer part of the detector can cause excessive triggers, so the Chooz Level 1 trigger will have additional trigger criteria.

trigger condition based on the number of PMT's fired is added.

It can be seen that adding the condition on the number of PMT's fired reduces the probability of triggering on an event of less than 1 MeV near the edge of the detector, while the efficiency in the central region is hardly affected. The condition on the number of PMT's fired raises the threshold of the Level 1 trigger for events near the PMT's, and will reduce the trigger rate from low-energy background in the outer parts of Region 2 of the detector.

5.2.2 Level 2 Trigger

Two Level 1 triggers within approximately 200 μs generate a Level 2 trigger (see Figure 5.7), indicating that a "neutrino-like" event has been seen, and that the acquisition electronics should be read out.

The logic for the Level 2 trigger will be implemented with a CAMAC module using FPGA's (Field Programmable Gate Arrays). This same module will also control the TDC and WFD stops, and contain clock registers that are latched

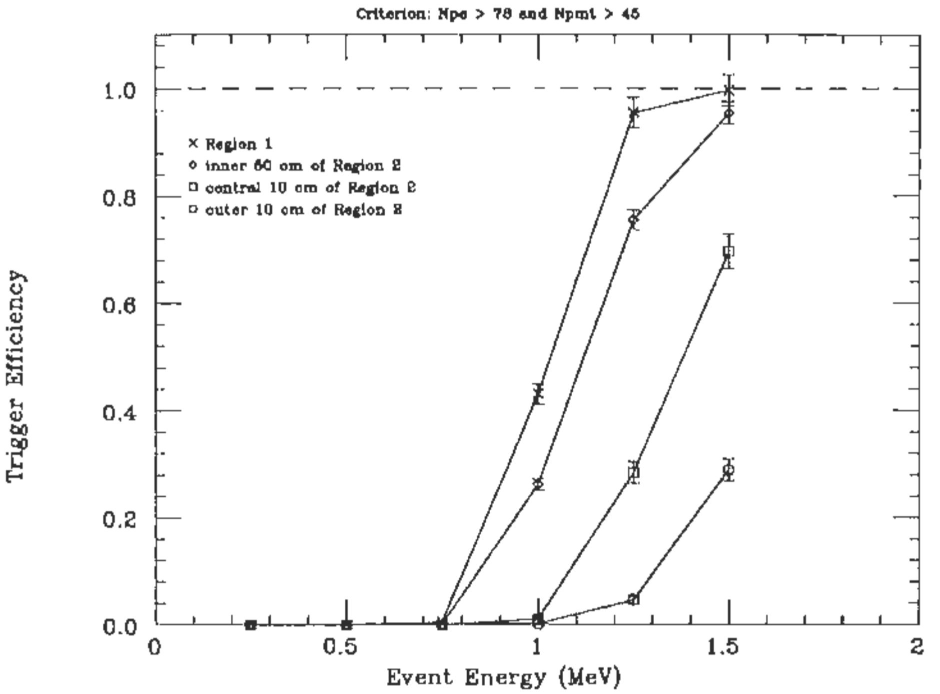

Figure 5.6: Efficiency as a function of energy shown for several regions of the Chooz detector, using a trigger criterion based on both the total number of detected photoelectrons and the number of PMT's participating in the event. The plot shows that this criterion reduces sensitivity to background in the outer regions of the detector and has nearly full efficiency for events in the inner volume.

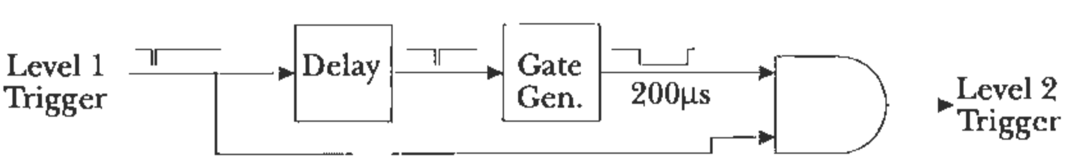

Figure 5.7: The Level 2 trigger is formed from two Level 1 triggers occurring within a time window of $200\,\mu s$. The implementation of the Level 2 trigger will use a digital counter to set the coincidence delay, with the logic contained on an FPGA (Field Programmable Gate Array).

for each Level 1 trigger so that the time between a pair of Level 1 triggers is recorded. Modules of identical design (but different FPGA programming) are used in the MACRO experiment to control readout of monopole triggers, and only a small amount of modification is required to adapt them for Chooz.

5.2.3 Veto and Other Triggers

A veto trigger will be used to tag through-going muon candidates in the veto counter (Region 3). The threshold of the veto trigger will be set at about 5 MeV (above the highest gamma energy) and would correspond to a muon track length of about 2.5 cm.

Other triggers, for example to do calibration, can be added very simply in the digital logic used for implementing the Level 2 trigger by reprogramming the FPGA's.

5.2.4 Trigger Summary

The planned trigger scheme uses the same low energy threshold for both the positron and neutron capture events, giving us sensitivity to neutron capture on hydrogen as well as on gadolinium. Information on hydrogen-capture events both inside and outside of the target volume may prove useful in understanding systematic effects in the detector. A further advantage of this trigger scheme is that it includes (accidental) events in which the neutron capture *precedes* the positron event, thereby allowing accurate determination of the chance coincidence rate,

Estimates of background radioactivity (see Figure 8.3) indicate a singles rate of approximately 100 Hz at a threshold of 1 MeV for Regions 1 and 2 together. Most of these events are in the outer part of Region 2, and it is expected that the Level 1 trigger rate will be somewhat lower due to the Level 1 trigger's higher threshold in the outer part of Region 2.

Coincident event rates, even with a 1 MeV threshold for both the positron and neutron signals, will be low enough that the overall event rate will be a few Hertz. The final positron and neutron energy and position cuts can then be made more accurately in offline analysis with full event reconstruction.

5.3 TDC's

High density commercial discriminators and TDC's will be used for the accurate determination of PMT pulse times (1 ns or better) needed to reconstruct the position of events. The TDC system can be implemented with either of two techniques, depending on the cost of the modules. There are a number of TDC modules from at least two vendors that have the necessary characteristics to be suitable for Chooz.

The first option for the TDC system is to use commercial multi-hit TDC's, so that both the positron and neutron pulses can be stored in the TDC for later readout. Fast-clearing of these TDC's is possible in the case of a single Level 1 trigger; however, the event pipeline within these multihit TDC's generally allows continuing without a fast-clear at the cost of a few extra hits to be read out of the pipeline on valid Level 2 triggers.

As a second option, we could use pairs of commercial "single hit" TDC's, so that one set of TDC's would record the positron pulse times and the other would record the neutron capture pulse times. To reduce dead-time from single Level 1 triggers, the roles of the two sets of TDC's can be alternated so that one of them is active while the other is being fast-cleared. This option requires intelligent control of the TDC stop and fast-clear inputs, the logic for which would be contained in the Level 2 trigger module and implemented within the FPGA's.

5.4 WFD's

The Waveform Digitizers (WFD's) for Chooz will give the pulse-height information for the PMT signals and the overall event history. Each input channel is sampled at 5 ns intervals with an 8-bit flash ADC. The output of the ADC is stored in a 64-byte ring buffer, giving a pulse shape history of 320 ns.

When the WFD receives a Level 1 trigger, the current buffer which contains the pulse shape information from the previous 320 ns is saved along with clock information, and the WFD continues sampling with a new 64-byte buffer. There are eight such pulse shape buffers, so the WFD can store eight independent pulses before the buffers are overwritten.

When a Level 2 trigger occurs, indicating that a "neutrino-like" event has been detected, a 150 μs delay occurs and then a stop signal is sent to the WFD's. The WFD's then stop taking data and the contents of their eight pulse shape buffers are available for readout. The delay between the Level 2 trigger and the WFD stop is to allow post-trigger pulses to be recorded. The pre- and post-trigger pulse histories stored by the WFD will be very useful in rejecting correlated background.

Figure 5.8 shows a block diagram of a single channel of the WFD system. The level of fan-in of PMT channels per WFD channel has not yet been determined; the use of individual TDC's on the PMT channels gives considerable flexibility in fanning in signals to the WFD's without degrading the event reconstruction.

The WFD system will be implemented in FASTBUS, because the large FASTBUS board size will allow two channels per card and also because it is well suited to supply the power requirements of the WFD cards.

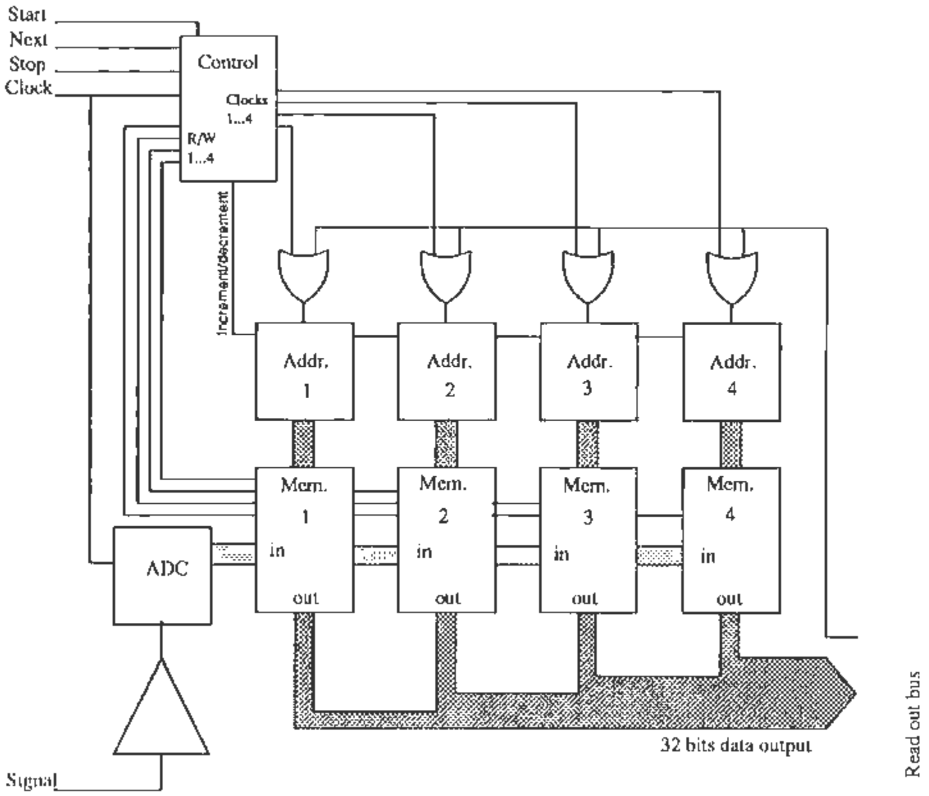

Figure 5.8: Block diagram of WFD system for use with Chooz. Only four of the eight pulse shape buffers are shown. The NEXT signal will come from the Level 1 trigger, indicating that a pulse should be stored, while the STOP signal is taken from the Level 2 trigger delayed by 150 μs. Each pulse shape buffer stores 320 ns of 8-bit pulse height at 5 ns intervals.

5.5 Acquisition System

The readout of the FASTBUS crates will be made by a commercially available FASTBUS module containing a 68020 microprocessor and an ethernet interface. This module will respond to trigger interrupts, and read out the WFD's and TDC's and buffer events. The use of zero suppression or event compression in the microprocessor is being considered.

Acquisition control, online display, and data storage will be performed by a local workstation connected to the FASTBUS microprocessor and other acquisition electronics.

Chapter 6

Calibration

The aim of the detector calibration is to permit reaching the 2% systematic accuracy desired for the neutrino event rate and energy spectrum measurements. In a long baseline reactor neutrino oscillation search, the event statistics tend to be relatively poor and, as a consequence, the neutrino energy spectrum analysis will not be very sensitive to oscillation parameters, except for large mixing. Maximum sensitivity to neutrino oscillations will be obtained by comparing the rate of detected neutrinos above a fixed energy threshold to the expected rate. The accuracy of the rate measurement is determined by knowledge of the e^+ energy threshold (including the two annihilation γ's) and of the neutron detection efficiency. Knowledge of the latter requires measurement of the absolute capture probability of a neutron by a Gd nucleus and of the efficiency of the selection criteria.

The various tasks of the detector calibration are:

- Monitoring the response of the digitizing electronics by means of calibrated charge pulses;
- Monitoring the gain of each PMT, which can be achieved by continuous on-line measurement of the single photoelectron peak amplitude, making use of the good energy resolution of the PMT's selected and by using information from the other calibration procedures;
- Determination of all parameters needed to calculate the energy deposition of each event from the recorded PMT pulse height and timing data. This task can be performed using γ lines from radioactive nuclei present in the background (^{40}K, ^{208}Tl, γ lines from neutron capture on Gd) or in dedicated source runs (^{65}Zn, ^{60}Co, ^{88}Y, Am/Be). These runs will be performed monthly, with daily checks to be made using a calibrated light pulse generator. In such a total absorption detector, γ lines will be easily observed and parameterized. The data needed for the energy calibration

are the light emission and transmission of the scintillator and the PMT and electronics response;

- Determination and monitoring of the neutron detection efficiency, including the Gd neutron capture probability and neutron capture time as well as the neutron selection criteria.

6.1 Energy Calibration

The mechanical design of the detector will include automatic introduction of various radioactive sources into the center of the gadolinium region by a movable lucite tube filled with scintillator for minimum optical interference. Another specially designed tube will permit exploration of other positions for checking radial energy dependence.

Two energy regions are worth monitoring accurately:

- The 2 MeV region associated with the e^+ threshold. For this region, standard γ sources exist (^{88}Y, ^{60}Co, ^{65}Zn) which will allow linearity measurement around the threshold.
- The other region is the energy window for the neutron capture signature (typically 5 – 10 MeV). The number of muon-tagged neutron captures in the Gd volume is small (several hundred per day) but enough for a daily check of the stability of the energy window and of the capture peak position. A dedicated Am/Be fast neutron source run will allow accurate determination of the neutron capture peak using the recoil proton pulse and the 4.4 MeV γ as a trigger. The 8 MeV capture peak can also be used as an energy calibration reference point which is near the end of the e^+ energy spectrum. The time needed for these runs is small, so the interval between calibration runs can be short.

6.1.1 Peak Position Dependence

For a given energy deposit, the total charge collected on the PMT's shows a radial dependence (see Table 6.1.1). This 10% radial variation can be compensated by corrections based on the reconstructed event position. The corrections themselves can be determined from careful source calibrations.

6.1.2 Calibration of Region 3 (Veto)

In the veto region the energy resolution will be limited by the geometry and by collection of only about 30 pe's/MeV. Nevertheless, calibration will be possible using the peak positions of various γ lines using either source runs or the natural lines coming out from the rock, esp. ^{208}Tl. Flanges on the cover of the main vessel will permit the introduction of radioactive sources as well as light pulses.

Distance from center	**large axis**	**small axis**
0	1	1
25 cm	1.004	1.007
50 cm	1.015	1.013
75 cm	1.020	1.036
100 cm	1.023	1.065
125 cm	1.030	1.120
150 cm	1.131	1.070

Table 6.1: Spatial variation of the light collection efficiency. Results of a Monte Carlo simulation with 160 EMI 9351 PMT's installed 80 cm away from the acrylic vessel. These calculations assume 8 m as the mean light attenuation length.

6.1.3 Short Term Gain Monitoring

We have two possibilities for monitoring the short term gain stability:

- Using the spark-gap system developed for the Bugey experiment [36]. This system consists of a nitrogen filled 30 Hz spark gap with special spherical tungsten electrodes. The device provides an intense blue pulse that is filtered to match the scintillator-photocathode combined photosensitivity (420 nm). The intensity can be adjusted by a CAMAC-controlled set of precision neutral density filters, which are also used for linearity measurements of the entire chain of electronics. To use this system for Chooz, we will have to provide an optical fiber to carry the light to the center of the gadolinium volume, and a light diffuser to illuminate the PMT's as homogeneously as possible. To obtain the needed accuracy quickly, we would need about 50 photoelectrons on each tube (equivalent to a 100 MeV energy deposit). This system would permit on-line equalization and stabilization of the gains of the 160 channels.
- Similarly, we could use a UV pulsed laser with a quartz fiber leading to the center of the detector. UV-induced fluorescence of the scintillator liquid would then provide an isotropic light source with the correct spectrum. We are currently investigating the feasibility of this solution.

In both solutions, dedicated photosensitive detectors are needed to monitor the amount of light provided by either the spark-gap or the laser, on a pulse-to-pulse basis.

6.2 Neutron Detection Efficiency Calibration

Good control of the neutron detection efficiency requires several types of information:

- measurement of the absolute neutron detection efficiency;
- monitoring the time stability of the neutron detection efficiency;
- determination of the spatial variation inside the Gd region; and
- measurement of the neutron capture time in the Gd region.

6.2.1 Absolute Efficiency Measurement

The absolute neutron detection efficiency will be measured in the center of the detector using the neutron multiplicity method with a ^{252}Cf spontaneous fission source ([37]). Even with fast neutrons, the size of the Gd region in the detector is large enough to catch all neutrons emitted by the source. We can therefore treat the detector as an infinite medium. Our electronics will permit full measurement of up to 7 neutrons from each tagged fission. The tagging is done by recording the signal created by the fission products either in a semiconductor or in a gas scintillation detector.

6.2.2 Time Stability of the Neutron Detection Efficiency

Time stability of the neutron efficiency is governed by the stability of the energy calibration, discussed previously, since it depends on the stability of the capture peak inside the selected energy window. The other parameter controlling the neutron detection efficiency is the Gd concentration in the scintillator, which can be checked either by measurement of the capture time of the neutron or by periodic absolute neutron detection efficiency measurement.

6.2.3 Uniformity of the Neutron Detection Efficiency

Uniformity of the neutron detection efficiency is linked to several parameters:

- Spatial variation of the energy response of the detector as discussed above. The capture energy of the neutron candidate can be corrected using knowledge of the reconstructed capture position. Furthermore, in this detector most of the energy of the γ's from Gd deexcitation will be absorbed. Small variations of the energy response of the detector will thus not lead to large efficiency variations. Moreover, we will directly measure the spatial response of the detector to neutron capture using an Am/Li low energy (200 KeV) neutron source.

- Losses of neutrons escaping the Gd region. This effect will be checked by scanning with the Am/Li source. This measurement will also be used to validate the neutron Monte Carlo code. The final correction must be calculated since it would also need to include neutrons created by neutrino interactions in the unloaded scintillator which diffuse into the Gd region. The correction is very small (~0.5%) and uncertainties in it will not be significant.

6.2.4 Capture Time Measurement

The capture time of the neutron will be measured during the Am/Be source runs using the prompt pulse (4.4 MeV γ and the thermalization pulse) as the time start. It can also be checked continuously by the neutrino data and by cosmic ray-induced neutrons.

Chapter 7

Event Rate and Statistical Error

We calculate the expected antineutrino event rate in the experiment to be about $30\,\mathrm{d}^{-1}$ using the assumptions shown in Fig. 7.6. For a 200-day run we thus anticipate about 4400 events, allowing statistical errors in the vicinity of 2%, assuming a good background measurement can be made before the first reactor starts operation in late 1995.

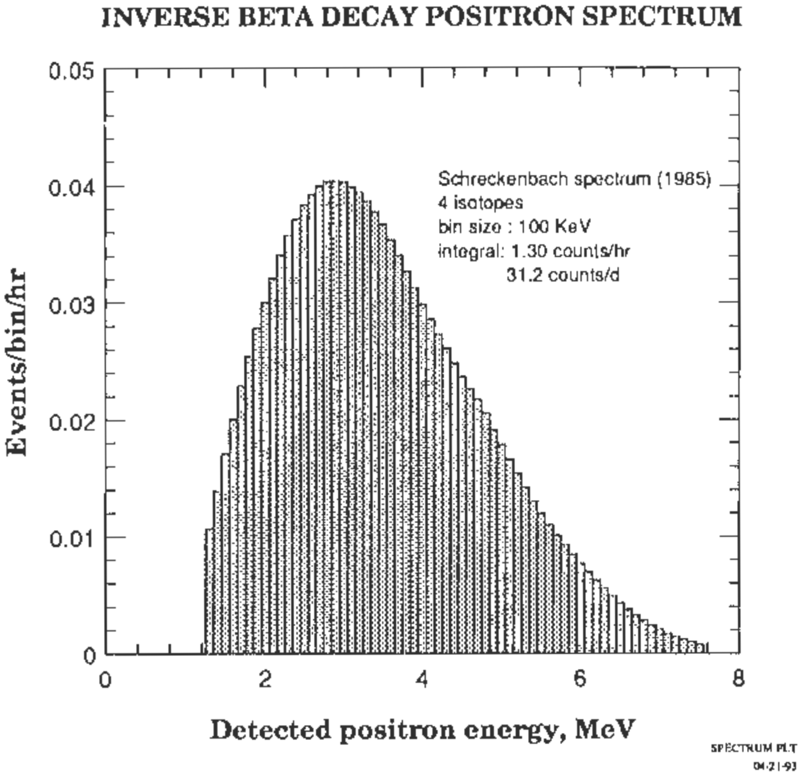

Figure 7.1: The inverse beta decay positron spectrum for Chooz, with a threshold cut at 1.3 MeV.

SUMMARY OF EXPERIMENTAL ERRORS ($1\,\sigma$)

Cross section and neutrino flux	2.5%
Reactor power + fuel composition	1.5%
Detection efficiency	2.0%
Systematic error	3.5%
Statistical error	2.0-4.0%
TOTAL ERROR	4.0-5.3%

Table 7.1: Estimates of systematic, statistical and total errors in the Chooz experiment.

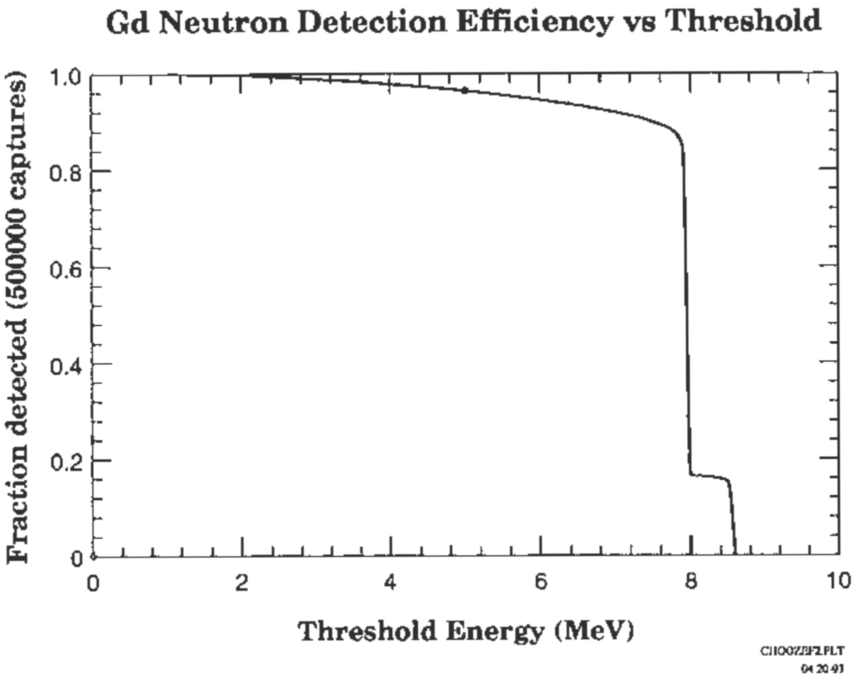

Figure 7.2: Calculated detection efficiency for gadolinium neutron capture events vs. threshold. At the expected operating threshold of 5 MeV, the efficiency will be 96.4%, as shown by the plotted point.

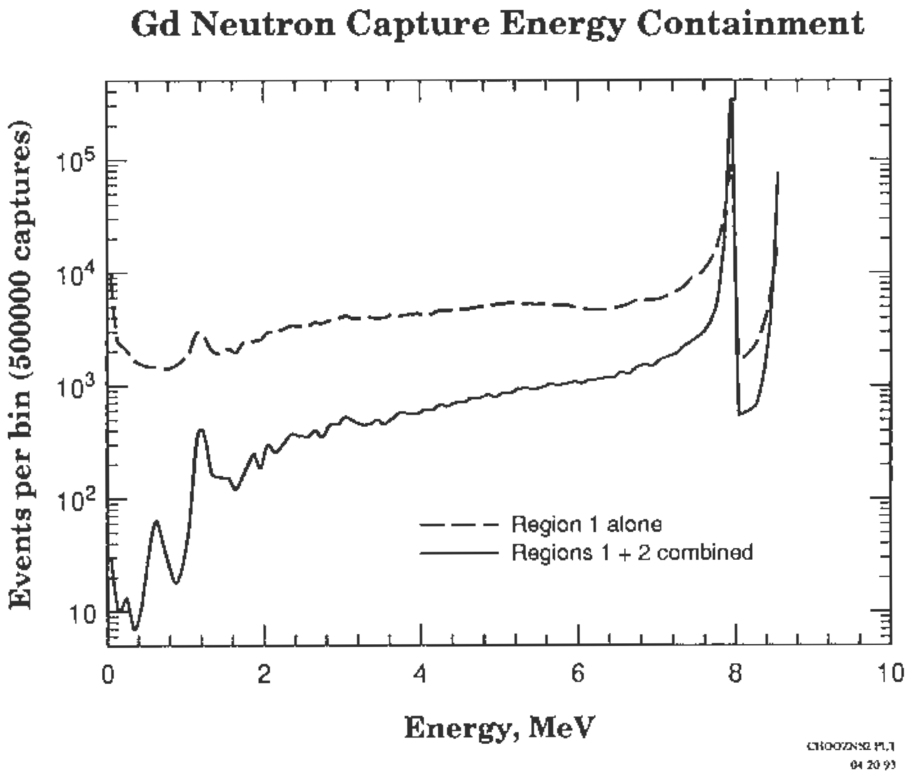

Figure 7.3: Containment of the energy deposited by gadolinium neutron capture gamma rays in the Chooz detector. The solid curve shows the effect of surrounding the target (region 1) with an energy containment volume (region 2): reduction by about an order of magnitude of the low energy tail caused by escaping gamma rays. The two peaks at 8.527 and 7.929 MeV are caused by the presence of two capturing isotopes (^{155}Gd and ^{157}Gd) with different Q-values.

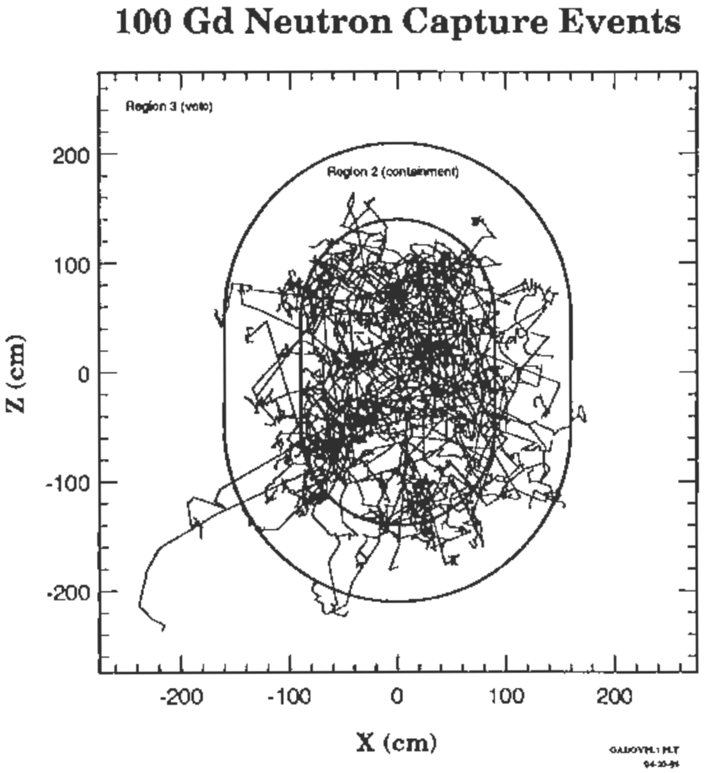

Figure 7.4: Trajectory plot for 100 Gd neutron capture Monte Carlo events. The source points are randomly distributed throughout the target (region 1). Each event releases several gamma rays whose energies add up to about 8 MeV. Most of the energy leaking out of the target is absorbed in region 2, the event containment volume. The efficiency for depositing more than 5 MeV in regions 1 and 2 is 96.4%, as shown in Fig. 7.3, where the results of 500,000 Monte Carlo events are plotted.

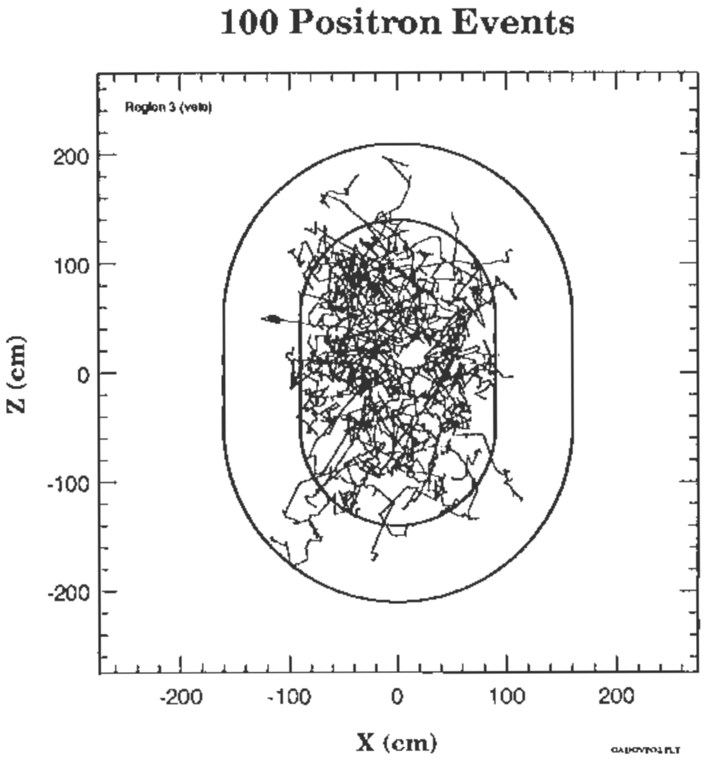

Figure 7.5: Trajectory plot for 100 positron Monte Carlo events. The kinetic and annihilation energies are almost perfectly absorbed in regions 1 and 2, with a calculated detection efficiency of 99.8%.

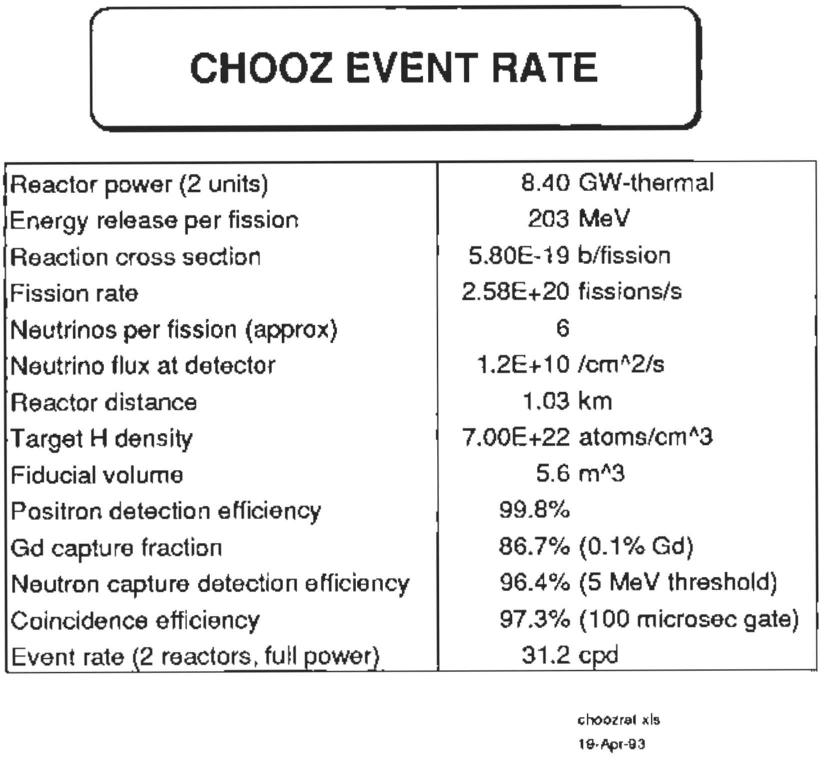

CHOOZ EVENT RATE

Reactor power (2 units)	8.40 GW-thermal
Energy release per fission	203 MeV
Reaction cross section	5.80E-19 b/fission
Fission rate	2.58E+20 fissions/s
Neutrinos per fission (approx)	6
Neutrino flux at detector	1.2E+10 /cm^2/s
Reactor distance	1.03 km
Target H density	7.00E+22 atoms/cm^3
Fiducial volume	5.6 m^3
Positron detection efficiency	99.8%
Gd capture fraction	86.7% (0.1% Gd)
Neutron capture detection efficiency	96.4% (5 MeV threshold)
Coincidence efficiency	97.3% (100 microsec gate)
Event rate (2 reactors, full power)	31.2 cpd

choozrat.xls
19-Apr-93

Figure 7.6: Calculation of the neutrino event rate.

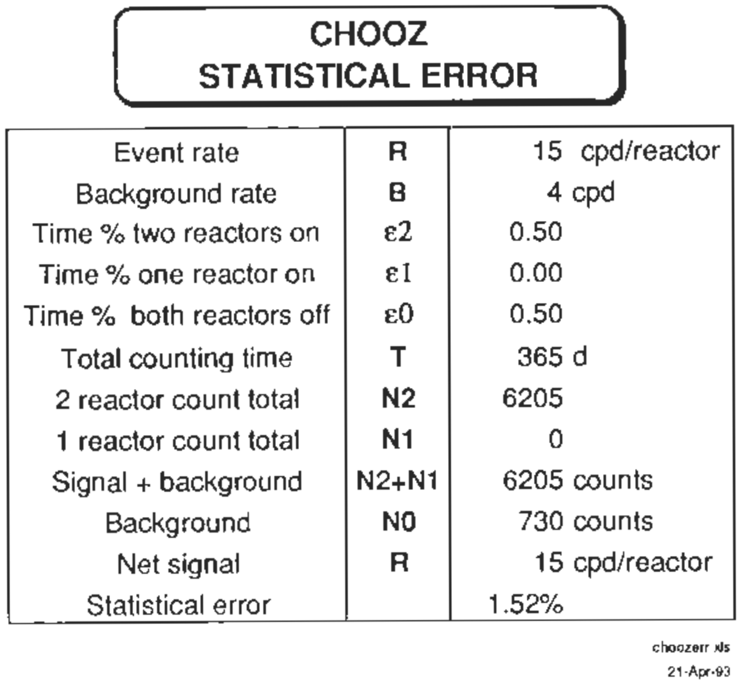

CHOOZ
STATISTICAL ERROR

Event rate	R	15 cpd/reactor
Background rate	B	4 cpd
Time % two reactors on	ε2	0.50
Time % one reactor on	ε1	0.00
Time % both reactors off	ε0	0.50
Total counting time	T	365 d
2 reactor count total	N2	6205
1 reactor count total	N1	0
Signal + background	N2+N1	6205 counts
Background	N0	730 counts
Net signal	R	15 cpd/reactor
Statistical error		1.52%

choozerr.xls
21-Apr-93

Figure 7.7: Calculation of the statistical error for a one year run with a background of four per day. Six months of counting are assumed with both reactors at full power and six months with both reactors off. Fig. 7.8 plots the statistical error for a range of background rates and reactor time-on fractions.

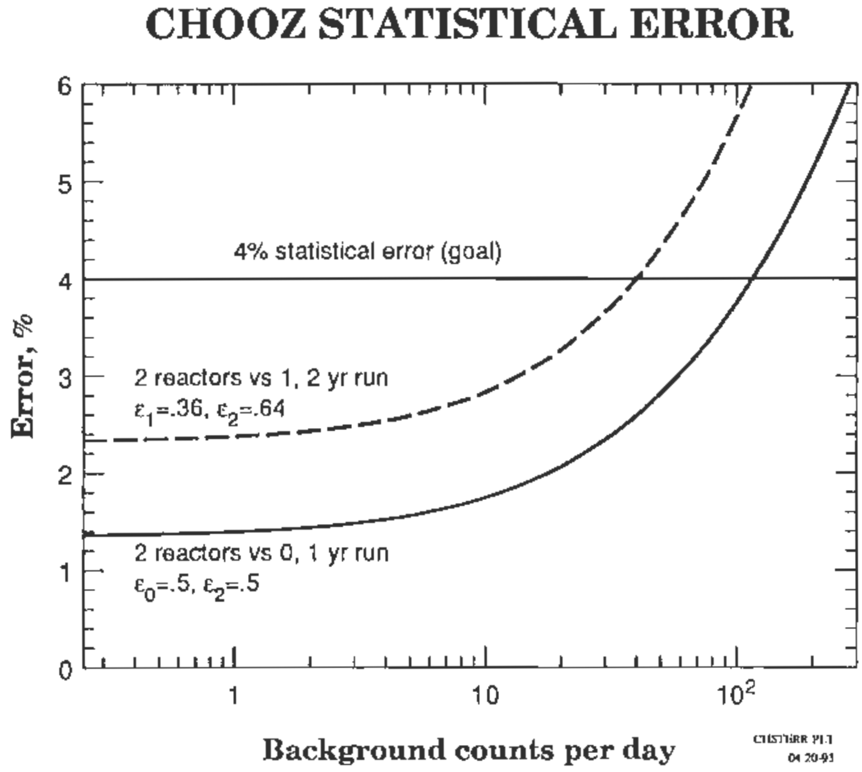

Figure 7.8: The statistical error for a range of background rates and reactor time-on fractions. Even for the less favorable case of no counting time with both reactors off and a single reactor time-on fraction of 80% (dashed curve), a two year run will achieve a 4% statistical error for background rates up to 40 per day. For the anticipated background rate of 4 per day, the same run would reach a statistical precision of 2.5%.

Chapter 8

Background

In this experiment the main signature of the neutrino interaction is based on a clean neutron signal, the level of the natural neutron background being much lower than that produced by γ's. The 8 MeV total energy γ rays released by neutron capture on a gadolinium nucleus are well above the highest energy of the natural γ background (^{208}Tl, 2.614 MeV). To accept a neutron candidate as a neutrino-induced neutron we must find in its history the prompt pulse corresponding to the e^+ signal and no other correlated signal indicating either a μ going through the detector or a multiple neutron event. We can define the following two classes of background which can simulate a reactor-neutrino interaction:

- ACCIDENTAL BACKGROUND corresponds to a coincidence between two uncorrelated signals — an e^+ ($E \geq 2\,\mathrm{MeV}$) and a neutron ($E \geq 6\,\mathrm{MeV}$) within the time ($\Delta t \leq 100\ \mu s$) and space window. Using the estimated e^+ singles rate (section 8.1) and neutron singles rate (section 8.2) the accidental background rate will be

  $$R_{e^+} R_n \, \tau = (150\,\mathrm{s}^{-1})(1/3600\,\mathrm{s}^{-1})(10^{-4}\,\mathrm{s}) = .015\,\mathrm{hr}^{-1} ,$$

  nearly 100 times lower than the anticipated event rate.

- CORRELATED BACKGROUND is produced by fast neutrons whose collisions on free protons simulate the e^+ signal followed by slow neutron capture on a Gd nucleus. These fast neutrons can be produced either by cosmic-ray μ interactions in the detector and the surrounding material or by spontaneous fission in these materials. Cosmic ray interactions in the detector (stopping μ's and μ nuclear spallation) will be easily eliminated using the tagging information provided by the veto layer of the detector during ~ 3 life-times of the neutron in the detector. The neutrons created by spontaneous fission or by μ's stopping in the material surrounding the detector (energy $\leq$ 10 MeV) will be absorbed in the scintillator (thickness $\geq$ 1.5 m) surrounding the inner vessel containing the Gd-loaded liquid scintillator. We are thus left with fast neutrons produced either by spontaneous fission in the detector (section 8.3) or by μ nuclear spallation in the raw material around the detector (section 8.4).

8.1 Singles Rate Estimate for e^+-like Signals

Due to the e^+ energy threshold (2 MeV), well above the ^{40}K line, the positron-like singles rate will be mainly related to the amount of thorium in the detector and in the surrounding material. This situation requires materials selection for the detector (liquid scintillator, mechanical structures and phototubes) and careful estimation of the effect of the U and Th content in the material surrounding the detector. Due to the level of U and Th in the rock of the tunnel (section 8.5), special shielding has been designed which will consist of selected low activity material filling the available volume between the rock and the main vessel (~ 70 cm thick). This material will probably be compressed sand (for example Comblanchien from the Burgundy area). The concentrations allowed are U $\leq$ 100 ppb, Th $\leq$ 100 ppb, ^{40}K $\leq$ 10 ppb. Using these numbers, the counting rate at the ^{208}Tl peak will be $\leq 150\,\mathrm{s}^{-1}$ inside the volume defined by the PMT's supporting structure (region I and II), to be compared to $\leq 20\,\mathrm{s}^{-1}$ from the PMT's and the liquid scintillator.

8.2 Singles Rate Estimate for n-like Signals

Neutron candidates can be produced by the following processes:

- real neutron capture by a Gd nucleus without a visible prompt pulse ($E_{visible} \leq 1$ MeV) produced by neutron thermalization; and by
- high energy γ's entering the volume defined by the PMT's (regions 1 and 2).

8.2.1 Thermal Neutron Capture

Thermal neutrons which reach the Gd-loaded liquid scintillator arise from the following two sources:

- spontaneous fission in the detector (section 8.3) — the rate is negligible ($\ll$ 1/h)

- cosmic-ray induced neutrons - the number can be deduced from the thermal neutron measurement at Bugey. This measurement was done with a detector made of a 2 m^3 vessel containing 254 ^{3}He counters and filled with water. Using data collected during the reactor shutdown, after alpha background subtraction and muon-tagged neutron rejection, we obtain $\simeq 60$ thermal neutron captures/m^3/h. Assuming pessimistically that all these neutrons were produced by cosmic ray interactions outside the active shielding, we can extrapolate to the conditions of the detector tunnel at Chooz, finding 2.6/m^3/h. Adding the improved shielding conditions of the Chooz detector, the number of neutron captures in the Gd target will be $\leq$ 1/h

8.2.2 High Energy γ's

The main source of high energy γ's is neutron capture in the rock. The source of neutrons is the (α,n) reaction in light elements, the α-particle being produced by ^{232}Th and ^{238}U contained in the rock. This effect has been calculated and measured in the Creighton mine for the SNO proposal. The flux of γ's with an energy ≥ 5 MeV is equal to 24/m^2/h, the quantity of ^{232}Th in the rock being 5.3 ppm at the location of the measurement. In our experimental conditions (low activity sand around the detector) the γ flux entering the detector will be 0.5/m^2/h. For these γ's the attenuation in the external layer of the detector is ~ 300 and so their counting rate will be $\leq$ 1/h in regions 1 and 2.

8.3 Spontaneous Fission

Spontaneous fission is determined by the abundance of natural uranium in the raw material of the detector — 1 gram of uranium produces 45 fissions/h. Taking into account the mean neutron multiplicity of 2.5 yields 112 neutrons/h. Using the measured values of the uranium content in the raw material of the detector (see Table 8.5), we can show that the main origin of fissions will be the PMT's and their supporting structure ($\leq$ .035 mg of natural uranium in the liquid scintillator). The upper limit for 200 PMT's will be

- PMT's: (70 ppb) · (600 gram) · (200) = 8.4 mg
- stainless steel: (4 ppb) · (3000 gram) · (200) = 3 mg

The neutron rate therefore will be 1.3/h. Taking into account the solid angle (0.5), absorption in the 70 cm of scintillator around the gadolinium target ($\sim 10^{-3}$), it is apparent that the rate of Gd capture for these neutrons will be negligible. In addition, the thermalization signal will have a low probability of satisfying the e^+ energy threshold.

8.4 μ-Induced Background

Neutron production has been studied at various depths [38], but it is difficult to determine from these studies the absolute number of neutrons reaching the Gd target, since there is no reliable Monte Carlo program for neutrons between 10 and 100 MeV. We prefer to use measurements done at Bugey at 10 and 25 mwe (see Fig. 8.1), and to extrapolate to the 300 mwe Chooz depth using the results of [38]. The numbers are summarized in the Table 8.1.

Experiment	**Muon Flux** $/\mathrm{m}^2/\mathrm{s}$	**Depth** mwe	$\mathrm{N}_{neutron}$ $/\mu/\mathrm{g}/\mathrm{cm}^2$	**Measured Rate** $/\mathrm{m}^3/\mathrm{h}$
Bugey, 40 m	79.0	10	$3.2\ 10^{-5}$	13.7 ± 0.4
Bugey, 15 m	30.0	25	$4.7\ 10^{-5}$	8.3 ± 0.5
Chooz	.4	300	$14.8\ 10^{-5}$	.35 (estimate)

Table 8.1: Estimate of the muon-induced correlated background.

The fast neutron rate for the Bugey detector geometry at the Chooz site is thus estimated to be $.35\,\mathrm{m}^{-3}\mathrm{h}^{-1}$. To find the expected rate for the Chooz detector geometry, we must take into account the extra thickness of the liquid scintillator buffer in which the neutrons will be absorbed (≥ 150 cm instead of 35 cm as at Bugey). We therefore expect an additional attenuation factor well above 10 for 10–100 MeV neutrons. Under these conditions, the background induced by μ nuclear spallation should be $\leq 0.1\,\mathrm{h}^{-1}$ in a $6\,\mathrm{m}^3$ target of Gd-loaded liquid scintillator, more than ten times below the expected neutrino event rate.

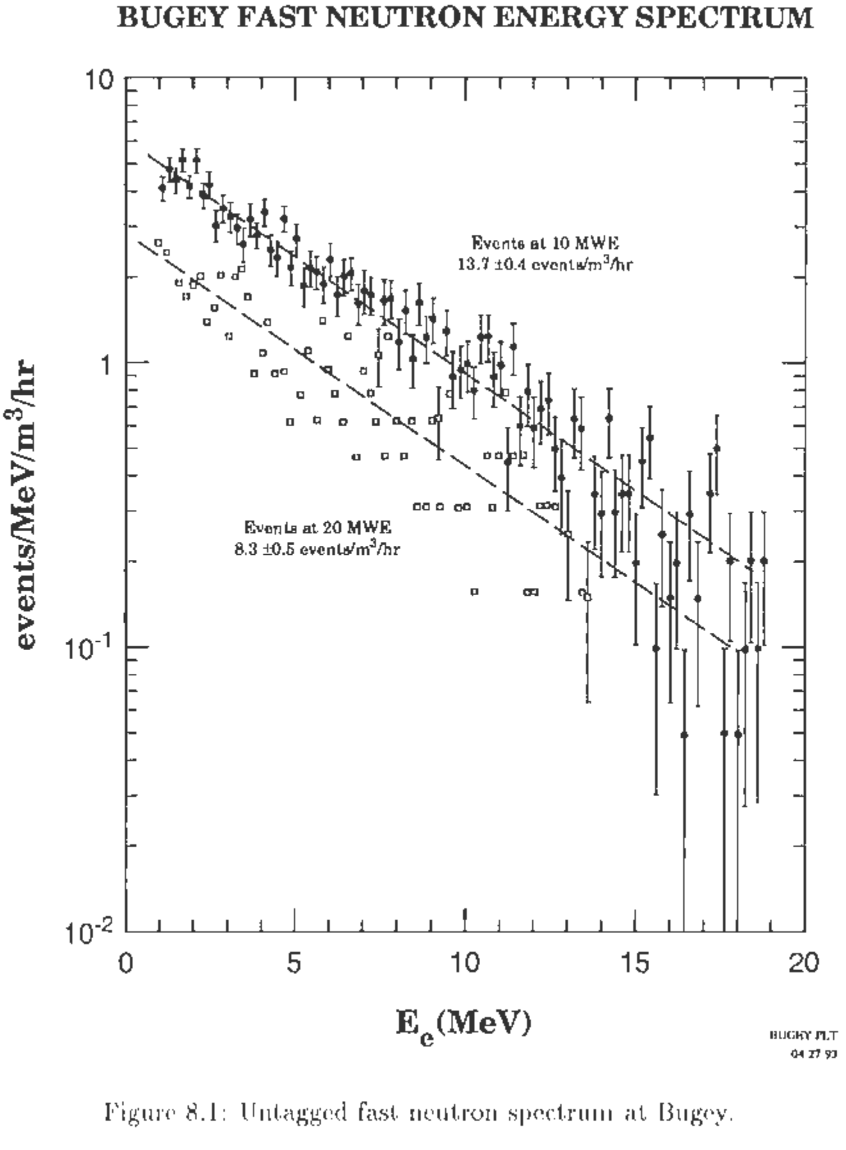

Figure 8.1: Untagged fast neutron spectrum at Bugey.

8.5 Activity of Shielding and Detector Components

	^{40}K	^{238}U	^{232}Th
schist	1.60 ppm	1.60 ppm	7.34 ppm
sandstone	.11 ppm	0.21 ppm	1.03 ppm
sand (Belgium)	.23 ppm	0.17 ppm	0.58 ppm
Comblanchien	20 ppb	0.50 ppm	113. ppb
iron shot (heavy concrete)	.18 ppb	$\leq$ 0.3 ppb	$\leq$ 1.7 ppb
iron plate (Bugey shielding)	$\leq$ .30 ppb	$\leq$ 2 ppb	$\leq$ 5 ppb

Table 8.2: Shielding Component Radioactivity

	^{40}K	^{238}U	^{232}Th
Gd	$\leq$ 5 ppm	0.7 ppb	5 ppb
PMT's (EMI) .600 kg each	20 ppb	70 ppb	100 ppb
stainless steel (typical)	$\leq$ 2 ppb	$\leq$ 0.4 ppb	$\leq$ 0.3 ppb
cable RG58CU (red)	0	17 ppb	0

Table 8.3: Detector Component Radioactivity

8.6 Summary of MC Singles Rate Calculations

INDIVIDUAL CONTRIBUTIONS
TO SINGLES RATE
ABOVE 1 MeV IN REGION 1

Material	**Th** Hz	**U** Hz	**K** Hz	**TOTAL** Hz
Gd-region 1	.034	.020	.013	.07
LS-region 1	.001	.003	.125	.13
LS-region 2	1.9E-4	5.7E-4	.025	.03
LS-veto	7.0E-6	1.0E-5	5.4E-4	5.6E-4
acrylic	1.1E-4	4.3E-4	2.0E-4	7.4E-4
PMT	.18	.19	.16	.53
steel tank	.0003	.0003	6.4E-7	.001
low activity gravel	.25	.34	.02	.61
schist/sandstone	.04	.04	.04	.12
TOTAL	0.5	0.6	0.4	**1.5**

conts101.xls
4/19/93

Figure 8.2: Individual contributions to the singles rate above 1 MeV in the target region. The most important sources of background are the photomultiplier tubes (.53 Hz) and the low activity gravel shielding (.61 Hz). The calculated total singles rate is 1.5 Hz.

CHOOZ DETECTOR SINGLES RATES

Nuclear Data

ISOTOPE	AMU	T-HALF (yr)	Isotopic abundance	Specific activity (bq/g)	Gamma's per decay (E > 200 KeV)
U238	238	4.51E+09	0.993	12239	1.81
Th232	232	1.41E+10	1.000	4044	2.40
K (nat)	39.1	1.28E+09	1.17E-04	30.3	0.11

Material Data			Contamination Levels		
Material	Quantity or Thickness	Mass (tons)	[Th] (g/g)	[U] (g/g)	[K(nat)] (g/g)
Gd-region 1	0.1%	.0049	5.0E-9	7.0E-10	1.0E-6
LS-region 1	5600 lit	4.9	1.0E-13	1.0E-13	1.0E-8
LS-region 2	19600 lit	16.7	1.0E-13	1.0E-13	1.0E-8
LS-veto	105500 lit	90.1	1.0E-13	1.0E-13	1.0E-8
acrylic	1 cm	.150	1.0E-12	1.0E-12	1.0E-9
PMT	150 tubes	.105	1.0E-07	7.0E-08	1.5E-04
steel tank	0.8 cm	9.6	1.0E-09	1.0E-09	1.0E-08
low activity gravel	74 cm	217	1.6E-07	7.1E-07	2.6E-04
schist/sandstone	40 cm	165	5.0E-06	2.0E-06	1.4E-02

Total Singles Rates (Hz)

Threshold Energy	Region 1	Region 2	Region 3
1 MeV	1.5	99	26824
1.5 MeV	0.7	39	11816
2 MeV	0.3	15	3242

contsum1.xls
4/19/93 18:07

Figure 8.3: Summary of the singles rates as calculated by the Monte Carlo gamma ray transport code. The contamination levels are measured (Gd, PMT, steel, low activity gravel and schist/sandstone) or estimated (liquid scintillator and acrylic). As shown in Fig. 8.2, the latter two materials are believed to contribute only about 10% of the total singles counting rate above 1 MeV in the target region.

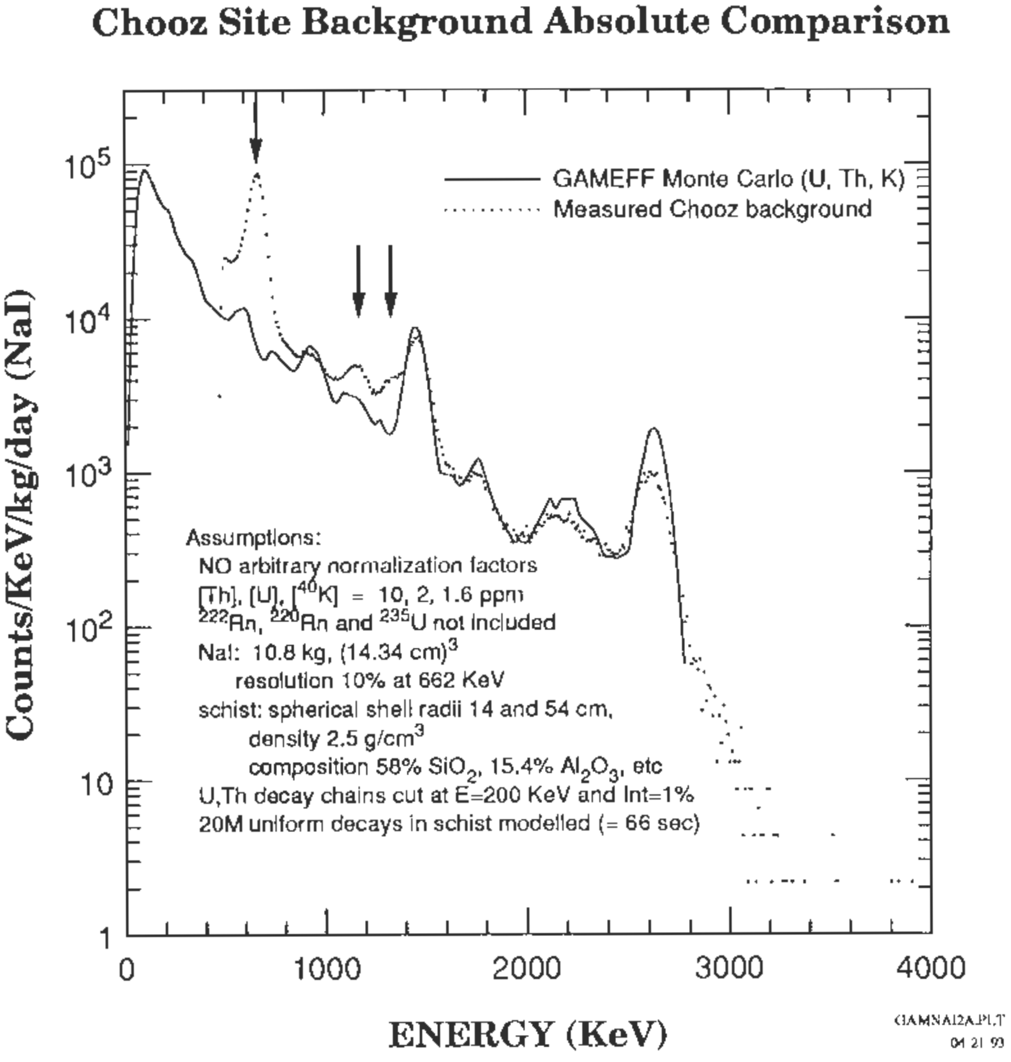

Figure 8.4: Comparison of the measured background at the Chooz underground site with a Monte Carlo simulation. The measured intensity of the 2.6 MeV ^{208}Tl line (thorium chain) is about a factor of two lower than the calculation, indicating that the true thorium content at the site is about 5 ppm. The potassium and uranium peaks are in good agreement with the calculation. The peaks at 662 KeV (^{137}Cs) and 1173 and 1333 KeV (^{60}Co) are caused by fission product contamination which will be cleaned up before the detector is installed. All three gamma rays are in any case nearly completely absorbed by the 74-cm low activity gravel shielding and by the 115-cm thick liquid scintillation veto counter and will not be troublesome.

Bibliography

[1] B. Pontecorvo, Sov. Phys. JETP **6** (1958) 429.

[2] Z. Maki, M. Nakagawa and S. Sakata, *Remarks on the Unified Model of Elementary Particles*, Prog. Theor. Phys. **28** (1962) 870.

[3] R. Davis *et al.*, Proc. 21^{st} Intl. Cosmic Ray Conf., (Adelaide, 1990) 7 155; J.K. Rowley *et al.*, in *Solar Neutrinos and Neutrino Astronomy* (AIP Conf. Proc. No. 126, 1985), ed. by M.L. Cherry *et al.*, p. 1.

[4] J.N. Bahcall and R.K. Ulrich, Rev. Mod. Phys. **60** (1988) 297.

[5] S. Turck-Chieze, *et al.*, Ap. J. **335** (1988) 415.

[6] K.S. Hirata *et al.*, Phys. Rev. **D44** (1991) 2241, Phys. Rev. Lett. **65** (1990) 1297, Phys. Rev. Lett. **65** (1990) 1301.

[7] A.I. Abazov *et al.*, Phys. Rev. Lett. **67** (1991) 3332; O.L. Anosov *et al.*, Proc. Neutrino '92, (Granada, 1992) (in press); V.N. Gavrin *et al.*, Proc. Intl. Conf. on High Energy Physics, (Dallas, 1992) (in press).

[8] P. Anselmann *et al.*, Phys. Lett. **B285** (1992) 376.

[9] P. Anselmann *et al.*, Phys. Lett. **B285** (1992) 390.

[10] J.M. Gelb *et al.*, Phys. Rev. Lett. **69** (1992) 1864.

[11] C.X. Chen and M.L. Cherry, Ap. J. Lett. **377** (1991) L105.

[12] J.N. Bahcall, *Neutrino Astrophysics*, (Cambridge Univ. Press, Cambridge, 1989).

[13] S.P. Mikheyev and A.Yu. Smirnov, Sov. J. Nucl. Phys. **42** (1985) 1441, Nuovo Cim. **9C** (1986) 17, Sov. Phys. Usp. **30** (1987) 759.

[14] L. Wolfenstein, Phys. Rev. **D17** (1978) 2369, Phys. Rev. **D20** (1979) 2634.

[15] M. Gell-Mann, P. Ramond, and R. Slansky, in *Supergravity*, eds. F. van Nieuwenhuizen and D. Freedman, (North Holland, Amsterdam, 1979) p. 315; T. Yanagida, Prog. Th. Phys. **B135** (1978) 66.

[16] R. Becker-Szendy *et al.*, Phys. Rev. **D46** (1992) 3720.

[17] K.S. Hirata *et al.*, Phys. Lett. **B280** (1992) 146.

[18] E.W. Beier *et al.*, Phys. Lett. **B283** (1992) 446.

[19] A. Acker, J.G. Learned and S. Pakvasa, *A Single Solution to the Atmospheric and Solar Neutrino Anomalies*, Phys. Lett. **B298** (1993) 149.

[20] T.K. Gaisser, *Cosmic Rays and Particle Physics*, (Cambridge Univ. Press, Cambridge, 1990) p. 103.

[21] F. Boehm *et al.*, *Experimental Study of Neutrino Oscillations at a Fission Reactor*, Phys. Lett. **97B** (1980) 310.

[22] Z.D. Greenwood *et al.*, *Updated Two-Position Results from the Irvine Mobile Neutrino Oscillation Detector*, Proc. Rencontre de Moriond, Les Arcs, France, 1987, (Ed. Frontières, Gif-sur-Yvette, France, 1987) p. 403.

[23] G. Zacek *et al.*, *Neutrino Oscillation Experiments at the Gösgen Nuclear Power Reactor*, Phys. Rev. **D34** (1986) 2621.

[24] G.S. Vidyakin *et al.*, *Detection of Antineutrinos in the Flux from Two Reactors*, Sov. Phys. JETP **66** (1987) 243.

[25] A.I. Afonin *et al.*, *A Study of the Reaction* $\overline{\nu}_e + p \rightarrow e^+ + n$ *at a Nuclear Reactor*, Sov. Phys. JETP **67** (1988) 213.

[26] G.S. Vidyakin *et al.*, Jour. Moscow Phys. Soc. **1** (1991) 85.

[27] E. Kajfasz. *Bugey III Neutrino Oscillation Experiment. Some Preliminary Results*, preprint CPPM-92-001, April 1992.

[28] F. Boehm *et al.*, *Reactor Based Neutrino Oscillation Experiments*, preprint CALT-63-647, Nov. 1992; and in *DPF92*, to be published.

[29] R. Steinberg *et al.*, *PERRY: A Reactor Neutrino Oscillation Experiment Sensitive to* $\Delta m^2 = 10^{-4}$ eV^2, in *DPF92*, to be published.

[30] G. Bellini *et al.*(eds.), *Borexino at Gran Sasso*, (Dept. of Physics, Univ. of Milano, August 1991).

[31] W.C. Louis (spokesman), *A Proposal to Search for Neutrino Oscillations with High Sensitivity in the Appearance Channels (LSND)*, LA-11842-P, (Los Alamos, August 1990).

[32] The SNO Collaboration, *Sudbury Neutrino Observatory Proposal*, SNO-87-12, (Queen's Univ., October 1987).

[33] P. Jagam and J.J. Simpson, *Measurements of Th, U and K Concentrations in a Variety of Materials*, Nucl. Instrum. Meth. **A324** (1993) 389-398.

[34] D. Dassie *et al.*, *Ultra Low Radioactivity Measurements in the Frejus Underground Laboratory*, (IN2P3, France, September 1991).

[35] H. Robertson, *PMT Waterproof Base*, internal SNO report, (private communication).

[36] J. Berger *et al.*, *Photomultiplier Gain Monitoring at the 1% Level with a Blue Light Pulser*, Nucl. Instrum. Meth. **A279** (1989) 343.

[37] Nucl. Sci. Eng. **80** (1982) 603-629.

[38] M. Aglietta *et al.*, *Neutron Flux Generated by Cosmic Ray Muons at 5200 hg/cm^2 Underground*, Nuovo Cim. **12C** (1989).

[39] A.A. Borovoi, Sov. J. Nucl. Phys. **37** (1983) 801.

[40] K. Schreckenbach *et al.*, Phys. Lett. **99B** (1981) 251.

[41] F. von Feilitzsch *et al.*, Phys. Lett. **118B** (1982) 162.

[42] K. Schreckenbach *et al.*, Phys. Lett. **160B** (1985) 325.

[43] A. Hahn, Phys. Lett. **B218** (1989) 365.

[44] Y.V. Klimov *et al.*, *Measurement of the Electron-Antineutrino Spectrum of a Nuclear Reactor*, Sov. J. Nucl. Phys. **52** (1990) 994.

[45] E. Kajfasz, *Bugey III Neutrino Oscillation Experiment – Some Preliminary Results*, Proc. Rencontre de Moriond, January 1992, (Ed. Frontières, Gif-sur-Yvette, France, 1992) p. 145.

[46] H.V. Klapdor and Metzinger, Phys. Rev. Lett. **48** (1982) 127.

[47] Kuvshinnikov *et al.*, *Measurement of the Cross Section for the $\overline{\nu}_e + p \rightarrow e^+ + n$ Reaction and the Axial Constant of β-Decay in a New Experiment in the Reactor at the Rovno Nuclear Power Plant*, Sov. J. Nucl. Phys. **52** (1990) 300.

[48] *Projet d'Installation d'une Expérience Neutrino sur le Site de Chooz A: Appel d'Offre du Gros Œuvre et Second Œuvre*. (Collège de France, Paris, March 1993).